CATS: The Hubble Constant from Standardized TRGB and Type Ia Supernova Measurements

D. Scolnic[1] , A. G. Riess[2,3] , J. Wu[1,4] , S. Li[3] , G. S. Anand[2] , R. Beaton[2,3,5] , S. Casertano[2], R. I. Anderson[6] ,
S. Dhawan[7] , and X. Ke[1]
[1] Department of Physics, Duke University, Durham, NC 27708, USA; daniel.scolnic@duke.edu
[2] Space Telescope Science Institute, Baltimore, MD 21218, USA
[3] Department of Physics and Astronomy, Johns Hopkins University, Baltimore, MD 21218, USA
[4] Kuang Yaming Honors School, Nanjing University, Nanjing, Jiangsu 210023, People's Republic of China
[5] Department of Astrophysical Sciences, Princeton University, Princeton, NJ 08544, USA
[6] Institute of Physics, École Polytechnique Fédérale de Lausanne (EPFL), Observatoire de Sauverny, 1290 Versoix, Switzerland
[7] Institute of Astronomy and Kavli Institute for Cosmology, University of Cambridge, Cambridge CB3 0HA, UK
Received 2023 April 20; revised 2023 July 12; accepted 2023 July 17; published 2023 September 5

Abstract

The tip of the red giant branch (TRGB) provides a luminous standard candle for constructing distance ladders to measure the Hubble constant. In practice, its measurements via edge-detection response (EDR) are complicated by the apparent fuzziness of the tip and the multipeak landscape of the EDR. Previously, we optimized an unsupervised algorithm, Comparative Analysis of TRGBs, to minimize the variance among multiple halo fields per host without relying on individualized choices, achieving state-of-the-art $\sim{<}0.05$ mag distance measures for optimal data. Here we apply this algorithm to an expanded sample of SN Ia hosts to standardize these to multiple fields in the geometric anchor, NGC 4258. In concert with the Pantheon+ SN Ia sample, this analysis produces a (baseline) result of $H_0 = 73.22 \pm 2.06$ km s^{-1} Mpc^{-1}. The largest difference in H_0 between this and similar studies employing the TRGB derives from corrections for SN survey differences and local flows used in the most recent SN Ia compilations that were absent in earlier studies. The SN-related differences total ~ 2.0 km s^{-1} Mpc^{-1}. A smaller share, ~ 1.4 km s^{-1} Mpc^{-1}, results from the inhomogeneity of the TRGB calibration across the distance ladder. We employ a grid of 108 variants around the optimal TRGB algorithm and find that the median of the variants is 72.94 ± 1.98 km s^{-1} Mpc^{-1} with an additional uncertainty due to algorithm choices of 0.83 km s^{-1} Mpc^{-1}. None of these TRGB variants result in an H_0 of less than 71.6 km s^{-1} Mpc^{-1}.

Unified Astronomy Thesaurus concepts: Distance measure (395); Hubble constant (758)

1. Introduction

The tip of the red giant branch (TRGB) is a waypoint in the evolutionary state for giant stars and offers a useful tool for measuring extragalactic distances (Lee et al. 1993; Serenelli et al. 2017; Beaton et al. 2018). Distances obtained via the TRGB have proven vital for grounding other physical measurements of nearby galaxies (McQuinn et al. 2021; Shen et al. 2021; Mutlu-Pakdil et al. 2022) and have led to a more thorough understanding of the structure of our local Universe (Shaya et al. 2022; Tully et al. 2023). Recently, it has also been employed as a centerpiece of some distance ladders used to measure the Hubble constant (H_0; Jang & Lee 2017; Freedman et al. 2020; Blakeslee et al. 2021; Anand et al. 2022; Dhawan et al. 2022; Jones et al. 2022). Results from this measurement are particularly interesting in light of the intriguing "Hubble tension," which is an empirical difference between direct measures of H_0 from the distance–redshift relation measured in the late Universe and its predicted value based on the calibration of ΛCDM in the early, pre-recombination Universe primarily via a calibration of the sound horizon (e.g., Planck Collaboration et al. 2020). Distance ladders that include the TRGB find values between two of the main tentpoles (directly using a ladder that includes Cepheids of 73 ± 1 km s^{-1} Mpc^{-1},

Riess et al. 2022, hereafter R22, and inferred using the cosmic microwave background of 67.4 ± 0.5 km s^{-1} Mpc^{-1}, Planck Collaboration et al. 2020). Some TRGB results (e.g., $\sim$70 km s^{-1} Mpc^{-1}; Freedman et al. 2020) are consistent with both to 1.5σ or less, while others are somewhat higher at $\sim$71.5–73 (Blakeslee et al. 2021; Anand et al. 2022; Jones et al. 2022). It is unclear whether these differences are due to statistical fluctuations or differences in TRGB measurements or arise from other parts of the distance ladder unrelated to the TRGB, but reconciling any potential differences is paramount for improving our understanding of the Hubble tension.

Our ability to grasp the significance of any differences in TRGB analyses is further complicated by the complexity of the measurement itself. The empirical tip is due to the abrupt end of the luminosity function of RGB stars, but in practice, the tip often appears fuzzy due to unavoidable contamination by asymptotic giant branch (AGB) stars, other younger populations, internal extinction, foreground contamination, photometric errors, and, in some cases, small number statistics. Edge detection is equivalent to evaluating an empirical derivative of a noisy function, so it often produces multiple peaks and the potential for ambiguity in the identification of the TRGB. Different TRGB measurement methods address this ambiguity using different choices of how the measurement is made. It is hard to evaluate how individual choices for the identification affect the determination of the Hubble constant without a systematic, algorithmic approach that considers how all such variations in the procedure propagate to H_0. This paper only

deals with edge detection such as with a Sobel-like filter as a method to measure the TRGB and does not touch upon potential systematics in the luminosity function fitting method (Méndez et al. 2002; Makarov et al. 2006; Wu et al. 2014), which are likely different and outside the scope of this work.

When TRGB measurements are used as part of the distance ladder, they are used in the first two rungs, first for an absolute calibration using a geometric measurement and then to calibrate the luminosity of a secondary distance indicator like a Type Ia supernova (SN Ia; Scolnic et al. 2022), surface brightness fluctuations (Blakeslee et al. 2021), or the Tully–Fisher relation (Kourkchi et al. 2022). A great deal of recent work has focused on the first rung and the determination of an absolute I magnitude of the TRGB, with most results falling within a range of $\sim -4.06 < I < -3.95$ mag (Capozzi & Raffelt 2020; Freedman et al. 2020; Blakeslee et al. 2021; Hoyt et al. 2021; Li et al. 2022).

Some differences in the calibration rung are likely astrophysical in nature, as differences at the ~ 0.1–0.2 mag level appear within a single host and seem to depend on the stellar populations being probed in a specific study (Wu et al. 2022; Anderson et al. 2023; Hoyt 2023); other calibration differences may be due to differences in the measurement process itself. It is therefore essential to consider how to rectify such differences between the first and second rung rather than selecting the sharpest edge-detection response (EDR). For example, recent papers (e.g., Jang et al. 2021; Hoyt 2023) discussed using the optimal fields among the many in the LMC or NGC 4258 that are available for calibration. While these choices may be well motivated to derive the most precise value for calibration purposes, they may create a difference in how the first- and second-rung galaxies are treated within the distance ladder. More specifically, the criteria used to select ideal fields may not be feasible to apply for more distant second-rung galaxies, or the very nature of the difference in photometry quality may produce systematics.

As a first step, in Wu et al. (2023, hereafter W23), we "trained" an unsupervised algorithm for measuring the EDR to yield internally accurate and precise TRGB measurements for a wide range of halo fields around a common host. This is a powerful approach for avoiding confirmation bias of supernovae (SNe) or H_0, as the algorithm was optimized independently of a subsequent application to determine the Hubble constant. In order to optimize the algorithm, we systematically varied the most widely employed algorithmic features for measuring the TRGB, such as spatial filtering to remove star-forming regions, parameters controlling the smoothing and weighting of the luminosity function, the use of color selection to define the RGB region, and the selection of the maximum in the response function identifying the tip. For the last element, we found that a very informative quantity is the contrast ratio R at the tip, i.e., the ratio of the number of stars 0.5 mag below versus above the tip. We varied the algorithm parameters to measure the TRGB in multiple halo fields for each of the galaxies observed as part of the GHOSTS program (Radburn-Smith et al. 2011); the goal was to identify the selections that optimize the consistency of the tip measurements across different fields for the same galaxy without prejudice regarding its actual brightness.

By this process, we recognized an empirical relation with 5σ confidence between the observed tip magnitude of a field and the measured contrast ratio R, defined above, that would produce apparent differences in the tip at the 0.05–0.1 mag level for typical fields. Differences in tip magnitudes of this order (at 5σ significance) have been reported based on variability-selected subsamples in the LMC by Anderson et al. (2023) and could point to population effects, e.g., related to age or metallicity. Stellar population synthesis models indicate that R is a function of both age and metallicity (W23), with younger populations containing more AGB stars (brighter than the tip) and lower values of R. We found that we are able to reach a dispersion as low as 0.03 mag field^{-1} (1.5% in distance) for very high R, and the dispersion increases rapidly as R decreases, showing that R is both an indicator of the quality of a tip measurement and its brightness. A standardization technique for the application of the TRGB may improve the consistency between the first and second rungs. This is important for eliminating the difficulty and vagaries of choosing which fields between rungs 1 and 2 are comparable.

We use the maser host NGC 4258 as our sole source of TRGB geometric calibration because its TRGB can be measured most consistently with that in SN Ia hosts. The LMC has too large of an angular extent to measure efficiently with the Hubble Space Telescope (HST), which is essential for a self-consistent TRGB calibration. A calibration based on the Milky Way (MW) is challenging because MW stars are not at a single uniform distance, although several attempts have produced useful results (Freedman 2021; Soltis et al. 2021; Li et al. 2022). We utilize HST photometry of host galaxies provided by the Color–Magnitude Diagrams/Tip of the Red Giant Branch (CMDs/TRGB) catalog within the Extragalactic Distance Database (EDD; Tully et al. 2009; Anand et al. 2021a), which provides photometry with uniform procedures across the full range of hosts and calibrators, effectively reducing the sensitivity of H_0 to experimental differences in photometry or flux-scale calibration. The companion paper by Li et al. 2023 (in preprint, hereafter L23) presents an analysis focused on the measurements in NGC 4258.

The structure of this paper is as follows. In Section 2, we present the color–magnitude diagrams (CMDs) and other properties of the TRGB fields in SN host galaxies and derive the tip brightnesses of each field. In Section 3, we describe the methodology to determine H_0 and present our baseline results. In Section 4, we discuss the variants in our analysis method and their impact on inferences of H_0. In Section 5, we discuss a comparison to literature results, and in Section 6, we present our conclusions.

2. Measurements

2.1. Comparative Analysis of TRGBs in SN Ia Hosts

To calibrate the SN Ia fiducial luminosity with the TRGB, we compiled a list of all SN Ia hosts for which deep halo imaging exists with the HST Advanced Camera for Surveys (ACS) in F814W and a bluer color (F606W or F555W) with the host imaging and SN measurements available at the time of this analysis. The majority of the hosts have already been included in the studies by both Freedman et al. (2019; CCHP) and Anand et al. (2021b; EDD; see Table 1 of both papers). There are two SNe that we add from 2021: a second SN in NGC 1448 (SN 2021pit; R22) and SN 2021rhu in NGC 7814 (Dhawan et al. 2022). Thus, the sample studied in previous papers includes a total of 17 galaxies hosting a total of 22 SNe, providing the second rung of the distance ladder. Most of the
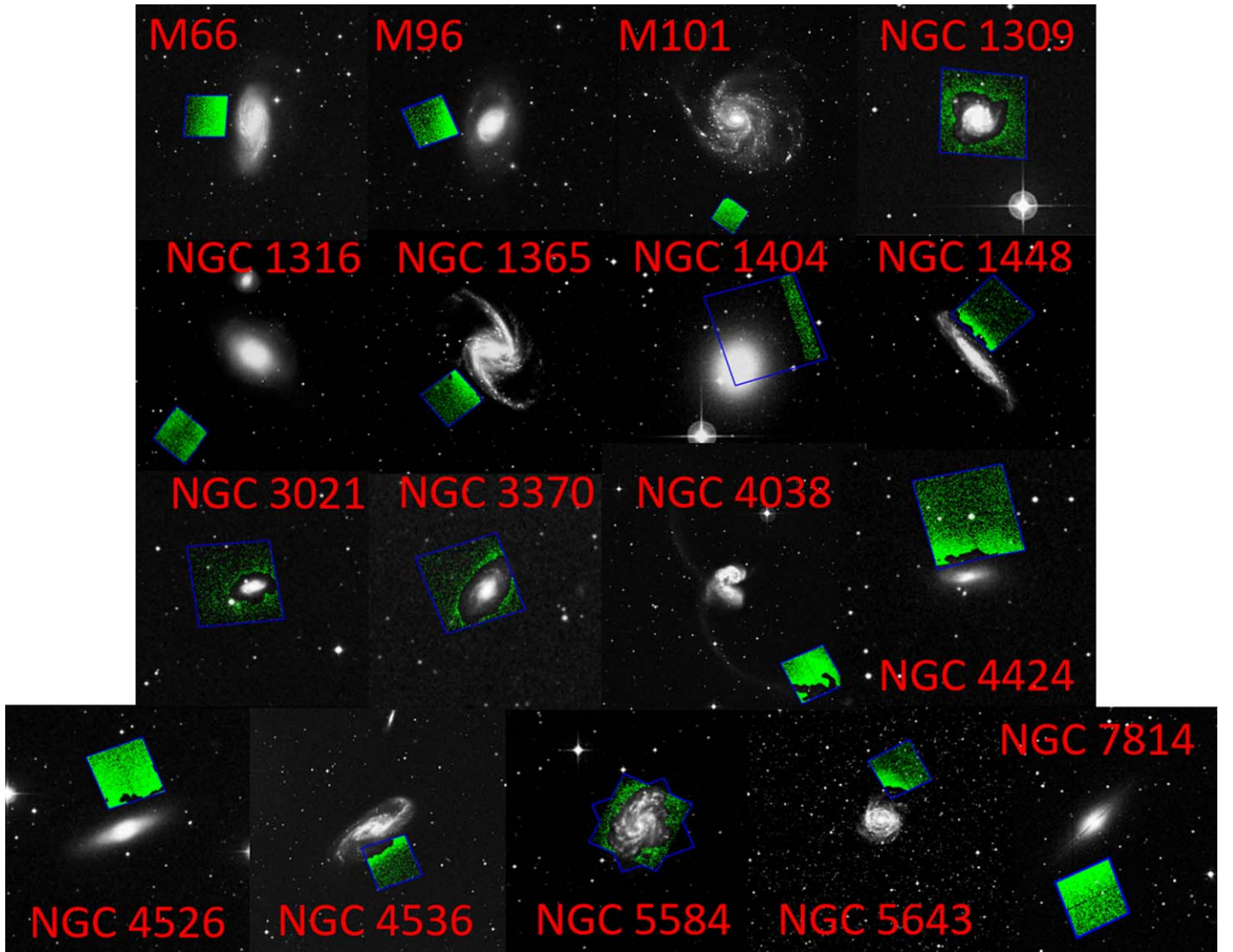
Figure 1. Footprints (shown with a rectangular outline) of the observed fields around galaxies used in the second rung of the distance ladder. The background images are from SDSS (Ahumada et al. 2020). A green dot is shown for each star that is included in the analysis of the CMD, with blank regions due to spatial masking of regions with high blue (young) star density as discussed in Section 2.1. An exception is NGC 1404, where we followed Hoyt et al. (2021), who showed that the field is severely crowded, and we only consider a similar halo strip.

data were explicitly obtained to measure the TRGB in the halo of the respective galaxies, although four hosts from the SH0ES programs (R22) were observed with the primary goal of obtaining Cepheid observations and had TRGB measurements performed by Jang et al. (2018). Two additional SN host galaxies, NGC 4038 and NGC 7814, were observed by HST programs 10889 and 10580 (I. Savianne). A parallel analysis of HST ACS images of NGC 4258 was carried out by L23.

As can be seen in Figure 1, the locations of the pointings relative to the disk/halo vary greatly among the different galaxies; while some pointings are well into the halo (e.g., M101 and NGC 1316), others have moderate to complete overlap with the disks or bulge (e.g., NGC 3021, NGC 1309, NGC 3370, NGC 5584, NGC 1404, and NGC 5643). For the purpose of limiting the TRGB measurement to exclusively older populations, these images are not all strictly from the halo and hence demonstrate the necessity of using an algorithm for excluding younger regions, which we can associate with blue main-sequence stars. We only analyze the photometry from Anand et al. (2021b), as the photometry used by

Freedman et al. (2019) has not been made publicly available. Anand et al. (2021b) performed point-spread function photometry with DOLPHOT (Dolphin 2016). Jang (2023) studied differences in the photometry of the TRGB when using the DOLPHOT or DAOPHOT packages (Stetson 1987; the method used by CCHP) and showed that there can be agreement of better than 0.02 mag, though the exact level of agreement depends on the specific reduction parameters used, as well as the corrections applied in postprocessing (e.g., aperture corrections). Thus, it is important to use a homogeneous photometry reduction within a single study.

The CMDs for all of the galaxies for which we can assess the tip are shown in Figure 2. To calculate the EDR (seen on the right of each panel in Figure 2), we employ the same automated algorithm to measure the TRGB here that was developed and optimized in W23 to produce the lowest TRGB dispersion for multiple fields in the same host for the GHOSTS sample. As seen in the CMDs of Figure 2, the sharpness of the TRGB peak varies significantly across fields, so it is important to maintain a robust algorithm for identifying the tip independent of external
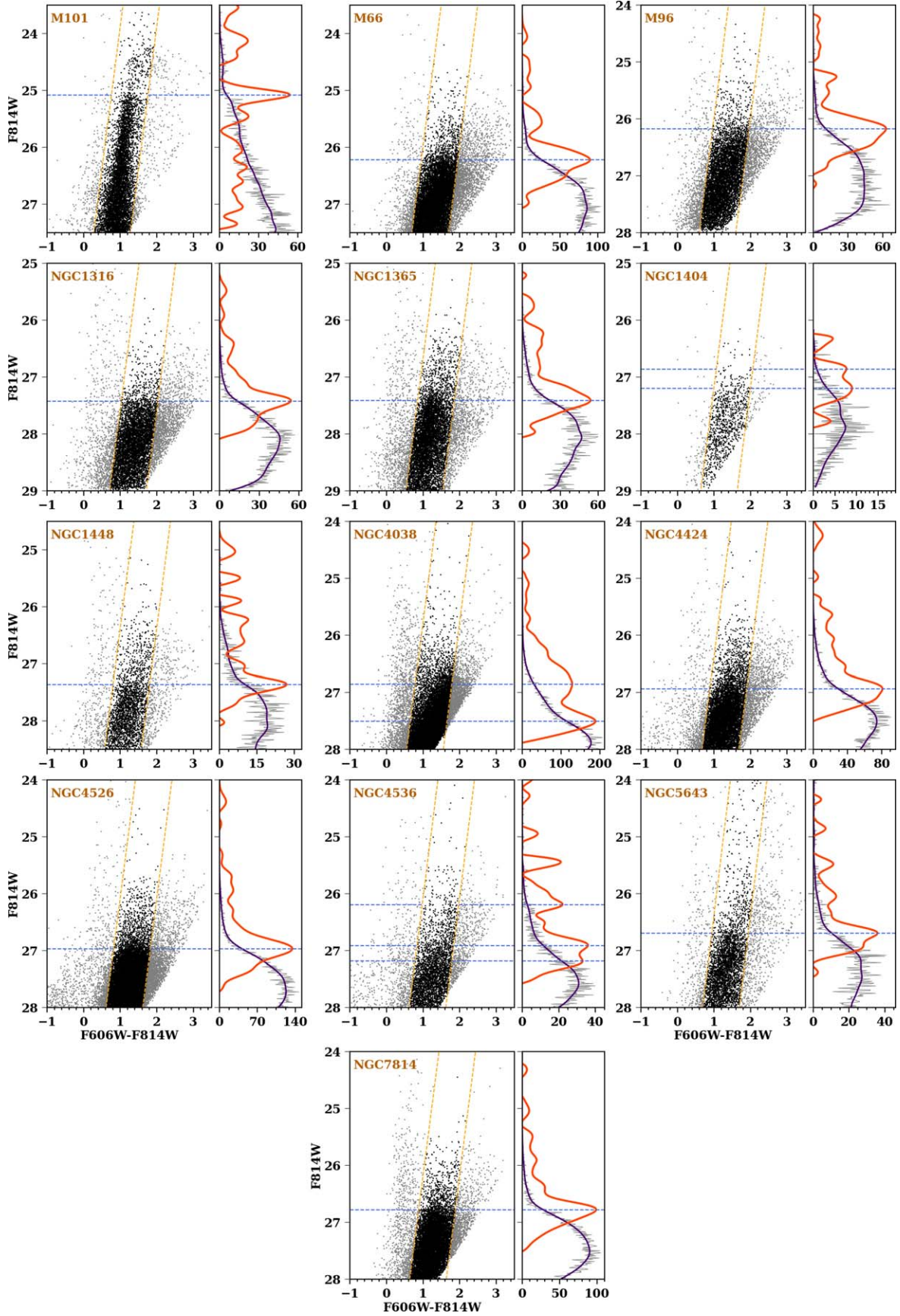
Figure 2. The CMDs of SN fields with significant tip detections ($R > 2$). In the left panel of each subplot, the orange lines show the color bands (i.e., selection region) for each field with a baseline 1.0 mag width, and the blue lines show the TRGB detections. In the right panel, the purple curve shows the smoothed luminosity function with a baseline smoothing scale of 0.1 mag smoothing width, while the red curve shows the EDR.

knowledge of the distance. We identify four primary features of a TRGB measurement algorithm, each of which is associated with a parameter that may be globally optimized. We describe them stepwise below; for all steps, we adopt the procedures discussed in W23.

2.1.1. Spatial Selection

Our first step is to perform a spatial selection of a usable region of a frame by automated detection and exclusion (masking) of young/blue regions parameterized by a frame-specific threshold. We identify the peak density of blue stars and then exclude regions of the frame whose density exceeds a modest fraction of this value, i.e., greater than *SpatialClip%*, where the blue star density is calculated in units of number of stars per 16 arcsec^2. From W23, *SpatialClip%* is set to be 10% of the frame maximum. A global minimum of 4 for the peak is used to contend with cases that have negligible blue stars because they are already far out in the halo. We identify the blue stars as those bluer than 0.3 mag in F606W–F814W color or 0.6 mag in F555W–F814W color. We adopt a significance threshold for detections of signal-to-noise ratio (S/N) >4, lower than the value of >10 used in W23; the reason is that this sample is generally at greater distances than the GHOSTS sample studied in W23, and the photometric uncertainties are evaluated differently by Anand et al. (2022) than in the GHOSTS analysis (Radburn-Smith et al. 2011).

The impact of the clipping is shown in Figure 1 and has the intended effect of reducing the overlap of the pointings with the disk area of each galaxy. The range of fractional field clipping is ~5%–20% for SN fields and ~20%–40% for NGC 4258 fields. In Section 4, we also present results obtained with double or half the clipping threshold. The typical number of stars is ~10,000 for SN fields and ~5000 for NGC 4258 fields due to the different distances.

2.1.2. CMD Range Selection

Second, we select a diagonal band of the CMD encompassing the RGB to measure the luminosity function. We introduce a parameter representing the width of the color band as *Width*. The optimal value of *Width* for the GHOSTS sample was found by W23 to be 1.0 mag. The center and slope of the band are varied for each frame to maximize the number of stars in the band. For most fields (and all of those used to measure H_0), both F606W and F814W data are available. We discuss four galaxies for which only F555W and F814W are available (bottom row of Figure 2 in more detail in the Appendix B). The range of allowed slopes is −7 to −5 for the CMDs with F814W versus F606W–F814W, and different slopes can be seen for the color bands in Figure 2.

2.1.3. Smoothing the Luminosity Function

The next step is to build a smooth luminosity function. We introduce a common parameter, *Smooth σ*, which is the size of the kernel for Gaussian smoothing. After creating the luminosity function from the CMD, we smooth the luminosity with a GLOESS with smooth σ mag for all galaxies. From W23, the optimal *Smooth σ* is set to be 0.1 mag.

2.1.4. Measuring the EDR

Finally, we measure the peaks of the EDR. We introduce the parameter *MinTh%*, which is the threshold relative to the peak edge detection for which other peaks would be included in the analysis. All tips are measured using a Sobel filter and Poisson weighting as described in Hatt et al. (2017). We retain all measured tip brightnesses whose EDR is greater than the *MinTh%* of the brightest peak detected. From W23, *MinTh%* is set to 60%. For each tip in each field, we measure its magnitude and contrast ratio, R, defined as the ratio of the number of selected stars that are 0.5 mag below the tip (i.e., in the RGB region) to those 0.5 mag above the tip (i.e., in the AGB region). In the next section, we will introduce the possibility of rejecting tips that are formal outliers among a universal relation (e.g., SN versus TRGB) that can contend with an unrelated feature like the tip of the AGB. We also define a value $N_{+,1.0}$ as the number of stars 1 mag below the tip.

Additionally, we correct the magnitude of each field by its MW extinction given by Schlafly & Finkbeiner (2011). For further tests, we also measure the mean color of the peak magnitude, the number of stars in the field, and the depth. We provide all of these values in Table 1. Furthermore, following W23, we also calculated the expected internal extinction based on Ménard et al. (2010, Equation (30)). Due to the typical distances of the fields from the center of the disk, the internal extinction estimates are generally ⩽0.02 mag and have a negligible impact on our conclusions (effectively canceling between the SN hosts and the fields of NGC 4258; see also Anderson 2022).

2.2. SN Ia Measurements from Pantheon+

For our distance ladder measurement, we use standardized SNe Ia in the second and third rungs. We make use of the compilation of redshifts and distances from the Pantheon+ sample as described in Scolnic et al. (2022) and analyzed for cosmological purposes in Brout et al. (2022a). A similar study by Freedman et al. (2020) used a mixture of literature-based SN Ia data for SNe in TRGB hosts (rung 2) and one specific survey only for SNe in the Hubble flow or third rung, the Carnegie Supernova Project sample. The need to combine disparate sources of SNe for rung 2 is unavoidable; SNe in this volume are rare, and their collection occurs over decades and many survey lifetimes. However, different sources of SN data may have differences in their photometric calibration that can be removed through the use of all-sky survey stellar catalogs and SN sample comparisons (Scolnic et al. 2015; Brout et al. 2022b). Even without such SN survey standardization, the presence of SNe from the same survey in both rung 2 and rung 3 will help cancel survey errors (Brownsberger et al. 2023) and is thus desirable.

Pantheon+ and other widely used compilations, such as JLA (Betoule et al. 2014), employ corrections to host redshifts (starting from the cosmic microwave background rest frame) to improve their convergence to the Hubble flow. These are based on well-sampled maps of the local flow (i.e., peculiar velocity) constructed from 2MASS. Pantheon+ also reassigns the host redshift to that of its host group or cluster when applicable, which further reduces the variance from the Hubble flow. Both steps have been shown to markedly improve the dispersion of the SN Ia Hubble diagram while lowering systematic errors in

Table 1
Summary of TRGB Parameters and Field Characteristics for Baseline Case

Galaxy	Field	Field R.A.	Field Decl.	Dist.	$m_{I,\mathrm{TRGB}}$	R	$N_{+,1.0}$	Tip Color	MW Ext.	Int. Ext.
SN Fields										
M101	M101	210.828	54.156	22.54	25.080 ± 0.111	4.4	1374.0	1.30	0.016	0.016
M66	M66	170.131	12.996	24.02	26.219 ± 0.041	6.1	7000.0	1.54	0.060	0.015
M96	M96	161.768	11.825	19.11	26.171 ± 0.040	6.7	3420.0	1.53	0.046	0.018
NGC 1316	NGC 1316	50.802	−37.323	70.92	27.421 ± 0.041	6.1	3682.0	1.56	0.038	0.006
NGC 1365	NGC 1365	53.464	−36.201	35.76	27.411 ± 0.204	3.8	4079.0	1.33	0.037	0.011
NGC 1404	NGC 1404	54.695	−35.568	10.31	26.860 ± 0.040	7.4	451.0	1.47	0.020	0.031
NGC 1404	NGC 1404	54.695	−35.568	10.31	27.200 ± 0.152	4.2	624.0	1.56	0.020	0.031
NGC 1448	NGC 1448	56.111	−44.604	63.17	27.362 ± 0.419	3.2	1768.0	1.33	0.025	0.007
NGC 4038	NGC 4038	180.360	−18.989	81.10	26.857 ± 0.192	3.8	9564.0	1.44	0.084	0.005
NGC 4038	NGC 4038	180.360	−18.989	81.10	27.507 ± 0.580	2.3	12,164.0	1.26	0.084	0.005
NGC 4424	NGC 4424	186.802	9.459	25.52	26.938 ± 0.151	4.0	6249.0	1.43	0.038	0.014
NGC 4526	NGC 4526	188.516	7.753	33.82	26.969 ± 0.043	5.6	10,368.0	1.37	0.040	0.011
NGC 4536	NGC 4536	188.588	2.145	25.58	26.193 ± 0.200	4.0	868.0	1.57	0.033	0.014
NGC 4536	NGC 4536	188.588	2.145	25.58	26.913 ± 0.364	3.3	2517.0	1.40	0.033	0.014
NGC 4536	NGC 4536	188.588	2.145	25.58	27.183 ± 0.676	2.3	2531.0	1.33	0.033	0.014
NGC 5643	NGC 5643	218.142	−44.115	19.84	26.694 ± 0.178	4.0	2345.0	1.46	0.306	0.018
NGC 7814	NGC 7814	0.814	16.071	28.83	26.780 ± 0.041	6.2	7498.0	1.40	0.081	0.013
NGC 4258 Fields										
NGC 4258	NGC 4258-1	184.829	47.333	18.49	25.360 ± 0.040	7.0	3193.0	2.07	0.030	0.019
NGC 4258	NGC 4258-1	184.829	47.333	18.49	25.690 ± 0.462	2.9	4529.0	2.00	0.030	0.019
NGC 4258	NGC 4258-10	184.607	47.209	33.16	25.268 ± 0.040	11.4	531.0	1.33	0.030	0.011
NGC 4258	NGC 4258-2	184.673	47.492	26.27	25.367 ± 0.108	4.4	1971.0	2.25	0.030	0.014
NGC 4258	NGC 4258-3	184.840	47.450	34.81	25.334 ± 0.130	4.4	480.0	1.98	0.030	0.011
NGC 4258	NGC 4258-4_G1	184.879	47.353	29.16	25.304 ± 0.048	5.4	1386.0	2.04	0.030	0.013
NGC 4258	NGC 4258-4_G2	184.918	47.320	33.05	25.288 ± 0.041	6.4	902.0	2.06	0.030	0.012
NGC 4258	NGC 4258-5	184.641	47.249	22.93	25.441 ± 0.040	6.7	2451.0	1.42	0.030	0.016
NGC 4258	NGC 4258-5	184.641	47.249	22.93	25.781 ± 0.567	2.6	3199.0	1.32	0.030	0.016
NGC 4258	NGC 4258-6	184.901	47.243	25.93	25.462 ± 0.040	6.4	4120.0	1.41	0.030	0.014
NGC 4258	NGC 4258-7	184.852	47.323	21.56	25.280 ± 0.040	7.5	3550.0	1.48	0.030	0.016
NGC 4258	NGC 4258-8	184.978	47.237	38.87	25.302 ± 0.040	7.2	474.0	1.29	0.030	0.010
NGC 4258	NGC 4258-9	184.977	47.332	44.33	25.320 ± 0.041	6.3	302.0	1.34	0.030	0.009

Note. The distance is given to the center of the galaxy in kiloparsecs. The TRGB magnitudes are raw and not corrected for extinction in this column. The $m_{I,\mathrm{TRGB}}$ values are the measured tip brightnesses, not the standardized values. Here R is the contrast ratio, and $N_{+,1.0}$ is the number of stars 1 mag below the tip. The tip color is in magnitudes from F606W–F814W. The MW extinction is from Schlafly & Finkbeiner ([2011](#)), and the internal extinction is calculated from Ménard et al. ([2010](#)).

H_0 and the equation of state of dark energy due to coherent flows (Carr et al. [2022](#); Peterson et al. [2022](#)).

It also common practice to apply quality cuts on the SN sample (Scolnic et al. [2018](#)) to limit systematic uncertainties due to the pull of "extreme" SNe (in color or light-curve shape) that are far from the middle of the distribution and whose standardization is thus likely to be less accurate. The most common selection is $-3 < x_1 < 3$ and $-0.3 < c < 0.3$ (Betoule et al. [2014](#); Scolnic et al. [2018](#), [2022](#)). Tighter limits empirically yield lower SN Ia dispersion on the Hubble diagram and are preferable when the size of the sample does not limit the statistics of the measurement; for example, the SH0ES analysis ([R22](#)) imposed tighter limits of $-2 < x_1 < 2$ and $-0.15 < c < 0.15$, and a number of the SNe in TRGB hosts would not pass these (1989B and 1998bu have $c \sim 0.3$, 1981D has $c \sim 0.2$, and 2011iv and 2007on have $x1 \sim -2$). As discussed in Rose et al. ([2022](#)), some SNe that fall out of the color cut are still quite well fitted by the SALT2 model and yield valuable distance measurements, although a study of SNe Ia with abnormal shape has not been done. To avoid limiting the already small TRGB host sample and better match the literature studies, we adopt the broader selection, which retains the two reddened SNe, 1998bu and 1989B, and the faster decliner, 2007on. In keeping with our unsupervised approach,

we retain all SNe within these bounds. We do not exclude a priori any tip measurements based on the inferred host distance; we will, however, exclude outliers at the $>3\sigma$ level in the subsequent global fit of the relation between SN magnitude and TRGB (see Section [3.2.2](#)).[8]

Besides the SNe in the Pantheon+ set, we also include ZTF SN Ia SN 2021rhu, which was recently discovered in NGC 7814 (Dhawan et al. [2022](#)). While the ZTF photometric system was not calibrated to PS1 in Brout et al. ([2022b](#)) due to its recent emergence, here we measure the mean difference of the ZTF Hubble flow and Pantheon+ sample. To do this, we utilize the public data release in Dhawan et al. ([2022](#)), and with the same SALT2 cuts as Pantheon+, we find agreement at the 0.02 ± 0.01 mag level, showing that there are no expected systematics that rival the statistical errors for including one SN measured by ZTF (Brownsberger et al. [2023](#)).

---

[8] Freedman et al. ([2019](#)) included SN 2007on in NGC 1404, as did Anand et al. ([2022](#)), though Freedman ([2021](#)) subsequently excluded it, citing an ~ 0.4 mag difference from its sibling in the same host, SN 2011iv, as well as its difference from SNe in NGC 1316, a galaxy that they presumed is at a similar distance as NGC 1404. In our baseline analysis, we find SN 2007on to be 1.9σ from the global SN–tip relation; hence, it is not excluded. We also note two other siblings in the TRGB host sample, 2021pit and 2001el, both in NGC 1448, with a similar-sized difference, so sibling rivalry at this level is not without precedent (Scolnic et al. [2020](#)).

Table 2
Summary of SNe Ia in TRGB Hosts

| SN	Host	m_B^0 (Error)	No. LC
2011fe	M101	9.808 ± 0.116	2
1989B	M66	10.980 ± 0.150	1
1998bu	M96	11.000 ± 0.150	1
1980N	NGC 1316	12.002 ± 0.097	1
2006dd	NGC 1316	11.940 ± 0.108	1
1981D	NGC 1316	11.610 ± 0.230	1
2012fr	NGC 1365	11.915 ± 0.119	2
2011iv	NGC 1404	11.974 ± 0.099	1
2007on	NGC 1404	12.460 ± 0.190	1
2001el	NGC 1448	12.254 ± 0.136	1
2021pit	NGC 1448	11.752 ± 0.200	1
2007 sr	NGC 4038	12.434 ± 0.112	2
2012cg	NGC 4424	11.496 ± 0.206	2
1994D	NGC 4526	11.532 ± 0.093	1
1981B	NGC 4536	11.551 ± 0.133	1
2013aa	NGC 5643	11.290 ± 0.102	2
2017cbv	NGC 5643	11.265 ± 0.079	2
2021rhu	NGC 7814	11.920 ± 0.150	1

Note. Standardized SN brightnesses from Pantheon+ for each SN used in this analysis. The number of light curves (LC) can be greater than 1 because the SN was observed by more than one survey.

In Table 2, we provide the mean standardized SN Ia magnitudes (denoted m_B^0) and their uncertainties for all of the SNe in the TRGB hosts. These magnitudes will be used to tie the TRGB brightnesses to the SN brightnesses in the second rung of the distance ladder, as discussed in Section 3.

3. Method and Nominal Results

3.1. TRGB EDR Standardization

In W23, we found evidence at the 5σ level of an empirical dependence of the measured tip brightness (i.e., the TRGB) and the previously defined contrast ratio, R. Independently, L23 found a slope of -0.015 ± 0.008 using 11 fields of NGC 4258, in good agreement with the slope found in W23 of -0.023 ± 0.0046. Combined, we find a slope of -0.021 ± 0.004, which we overlay on the data samples shown in Figure 3. We show that a similar relation may also apply to the 25 ranked LMC fields analyzed by Hoyt (2023), where we use the tip values from Hoyt (2023) and calculate the R values from the catalog and regions provided. The R found here correlates to some extent with the field rank discussed in Hoyt (2023), which was shown in that study to correlate with tip brightness. As shown in L23, there is also theoretical support for this relation; if the CMDs extracted from MIST isochrones (Choi et al. 2016) using different ages and metallicities are subjected to the same noise and measurement procedure at the level of half to the full empirical level, the resulting tip brightnesses correlate with the ratio of RGB to AGB stars. Some of this relation may be the result of the measurement process itself; the more asymmetric the population near the break, and thus the higher the contrast ratio, the more stars will "spill" to the bright side of the break, thereby increasing its brightness. This was also shown by Anderson et al. (2023), both by simulating luminosity functions and by empirically different TRGB magnitudes resulting from two individual sequences of variables that otherwise blend into the RGB. Regardless of whether this relation is driven by astrophysical or
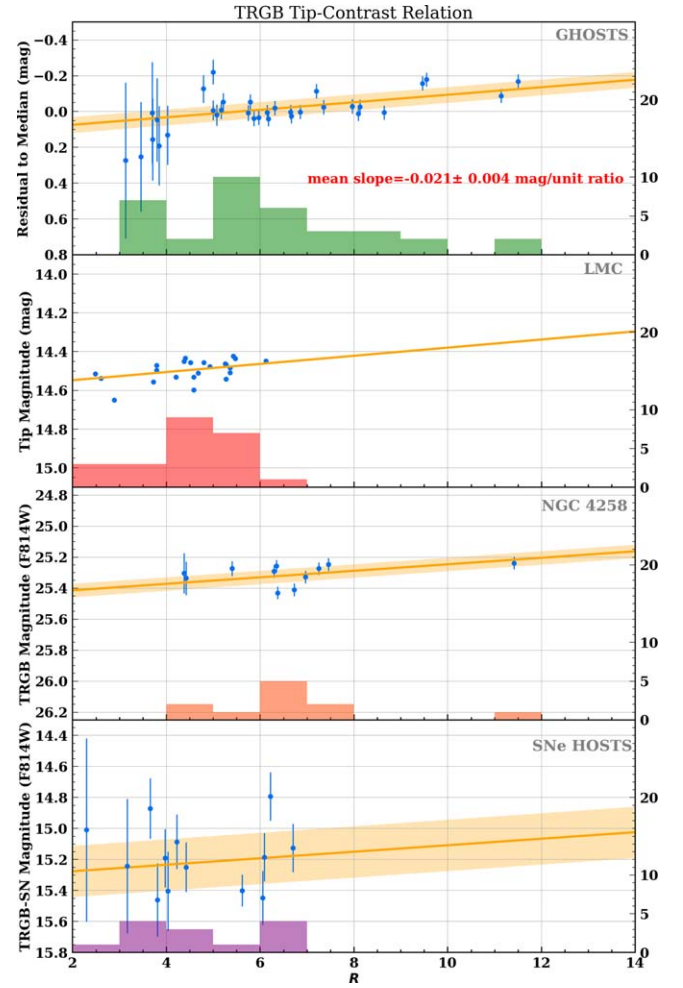
Figure 3. The TCR relation for GHOSTS (first panel), LMC (second panel), NGC 4258 (third panel), and SN host (fourth panel) galaxies. We do not include uncertainties for the LMC points, as the values are taken from Hoyt (2023) and did not apply the same CATS algorithm for measuring tip brightness.

measurement effects, an accurate measurement of H_0 requires the standardization of the tip brightness between rungs of the distance ladder. Therefore, to avoid a bias that would occur if the mean value of the contrast, R, is different in SN hosts than in NGC 4258, we use the contrast ratio to rectify the tips.

Since this relation is consistent between the NGC 4258 and GHOSTS samples (W23), we apply their mean linear correction for the tip-contrast relation (TCR) to remove the slope dependence. We must choose a fiducial (but arbitrary) R value to correct to a standard tip. We choose the value of $R = 4$ because it is near the middle of the SN host values (median $R = 4.2$, mean $R = 4.5$), making it a useful reference calibration.

Therefore, we can derive a standardized tip magnitude of each field measurement $m_{I,\mathrm{TRGB}}^{R=4}$ using the measured "raw" tip magnitude $m_{I,\mathrm{TRGB}}$ such that

$$m_{I,\mathrm{TRGB}}^{R=4} = m_{I,\mathrm{TRGB}} - 0.021(R - 4). \quad (1)$$

We note that the reference value of $R = 4$ has no effect on the determination of H_0 as long as the value is the same for the correction in the first and second rungs. In Section 4, we will also provide results without use of the TCR or R in general to determine its impact on H_0. Finally, we use the empirically

measured tip uncertainty model produced in W23, which, depending on R and $N_{+,1.0}$, are the specific values for the field, which is

$$\sigma = \sqrt{\left[\left(\frac{2e^{1.5(3-R)}}{e^{1.5(3-R)} + 1}\right)\left(\frac{1}{N_{+,1.0} - 100}\right)^{0.1}\right]^2 + 0.04^2} \text{ mag.}$$

(2)

Plots showing the dependence of the uncertainty on R and $N_{+,1.0}$ are given in W23. As the formula shows, there is a dramatic loss in precision for very fuzzy (low-contrast) tips with $R < 3$, and those with $R < 2$ have effectively no value. We therefore exclude from consideration tips with $R < 2$ as either spurious or of no weight.

We find that the four most distant hosts, NGC 5584, NGC 1309, NGC 3370, and NGC 3021 (based on their SNe), do not yield a tip with $R > 2$ at any location within a magnitude of the expectation from their SNe, including the magnitude indicated by Jang & Lee (2017). As discussed in Appendix B, this is a strong empirical qualification that is independent of the specific detection methodology; due to its low contrast, the uncertainty in the tip magnitude, at any plausible magnitude, is too low for it to carry any significant weight. This is not surprising because, given the observations of these four galaxies, there is a very small useful region for a clean TRGB measurement; the original observations targeted the disk in order to measure Cepheids, leaving very little area free from disk contamination. This is consistent with the finding by Anand et al. (2022), who also found no meaningful break in the luminosity function of these hosts using luminosity function fitting. We cannot readily attribute this difference from Jang & Lee (2017) to a difference in depth due to the photometry tools (we use DOLPHOT; Jang & Lee 2017 used DAOPHOT) because (1) they are based on the same images, (2) they both use image stacks to produce a full source list, and (3) the depth of the DOLPHOT photometry matches the expectation based on the HST exposure time calculator. Furthermore, the photometry catalog of Jang & Lee (2017) is not available, so a further understanding of this difference cannot be reached.

3.2. Determining H_0

The determination of H_0 from a three-rung ladder (connecting the geometric distance to NGC 4258, standardized TRGB, and standardized SN Ia) can be succinctly determined by measuring a single quantity for each rung independent of the others. While distance ladder analyses like Riess et al. (2022) measured covariances between the three rungs, the approach we are taking by measuring each rung separately favors transparency and ease of comparison to other studies, which we think is paramount for the TRGB method at this juncture. There is a very small loss of information by forgoing the use of nondiagonal covariance of SNe between rungs 2 and 3 and the simultaneous optimization of the TCR between rungs 1 and 2 with the present use of the GHOSTS sample (W23).

3.2.1. First Rung

The first rung entails the geometric calibration of the TRGB,

$$M_{I,\text{TRGB}}^{R=4} = m_{I,N4258,\text{TRGB}}^{R=4} - \mu_{0,N4258},$$

(3)

where $\mu_{0,N4258}$ is the geometric distance to NGC 4258 and $m_{I,N4258,\text{TRGB}}^{R=4}$ is the apparent TRGB in NGC 4258 in the HST

ACS F814W bandpass, rectified to a fiducial contrast ratio of $R = 4$.

The geometric measurement of $\mu_{N4258} = 29.397 \pm 0.0324$ mag is from Pesce et al. (2020), and the value of $m_{I,N4258,\text{TRGB}}^{R=4} = 25.361 \pm 0.0136$ mag is from L23. We note that the 11 halo or partial halo fields in NGC 4258 analyzed by L23 have individual apparent tips with meaningful contrast ratios in the range $4 < R < 11$ with a substantial range of $m_I = 25.6$–25.3 mag. The range in both contrast ratio and tip magnitude and their correlation illustrate the need for standardization to a common reference R. This avoids a subjective selection of a subset of tip values that may not match the properties of tip measurements in SN hosts. The value we adopt from L23 includes a small mean correction for extinction within NGC 4258 (following Ménard et al. 2010) of $A_I = 0.013$ mag and a mean correction for MW extinction of $A_I = 0.029$; for comparison with literature values without any extinction correction or TCR standardization, e.g., Jang et al. (2021), the uncorrected mean tip magnitude of all tips in all fields in NGC 4258 is 25.40 ± 0.047. Alternatively, weighting the simple, uncorrected tips by the number of stars below the tip yields 25.47. We then calculate a fiducial tip luminosity of $M_{I,\text{TRGB}}^{R=4} = -4.030 \pm 0.035$ mag, or $M_{I,\text{TRGB}}^{R=4} = -4.018 \pm 0.035$ without internal extinction. For comparison to studies without internal extinction correction or standardization (i.e., contrast weighting), i.e., a simple average of all NGC 4258 fields correcting only for MW extinction, this would be $M_{\text{F814W}} = -4.026 \pm 0.050$ mag (though at a mean R of ~6.6). Alternatively, if we treat the average of the tips as derived from a superposition of fields, i.e., as though it was a more distant host with a single field, we weight the tips by the number of stars below the tip, which yields an average correction for MW extinction of $M_{\text{F814W}} = -3.956 \pm 0.050$.

3.2.2. Second Rung

The second rung can be measured from the mean of a single apparent quantity, the difference between the standardized TRGB, $m_{I,\text{TRGB}}^{R=4}$, and the standardized SN magnitude, m_B^0, in the same galaxy. If a galaxy has multiple SNe, we use their average magnitude, $\overline{m_B^0}$. Because this term is the difference of two standardized candles in the same host, it is expected to be a constant across the sample. We will call this quantity ΔS:

$$\Delta S = m_{I,\text{TRGB}}^{R=4} - \overline{m_B^0}.$$

(4)

Then $\overline{\Delta S}$ is the value of ΔS averaged over the individual hosts, with weights that are the sum of the inverse error squared for each component. The values of m_B^0 are taken from Pantheon +, as discussed in Section 2. In cases where there are two SNe per host, we take the weighted mean and its error, and for three SNe per host, we take the error as their internal dispersion divided by $\sqrt{N - 1}$.

The GHOSTS survey sample used to develop the Comparative Analysis of TRGBs (CATS) algorithm had the benefit of multiple fields per host, so we could exclude "outlier tips" that were too far from the host mean. The same is possible in NGC 4258 with its 11 fields (L23). Past literature studies have referred to specific TRGB measurements as being "unsuitable" on a case-by-case basis, relying either on subjective factors, such as appearance, or on external information, such as an H I map for contamination from a young population, which may not be uniformly available along the distance ladder. Nevertheless, it may be worthwhile to exclude some TRGB or SN

measurement that appear anomalous in value. For the second rung, ΔS can serve this function because it has a constant expectation value for all hosts, so it can be used to identify true outliers. We adopt a 3σ ($\chi^2 > 9$) cut in the computation of the weighted mean $\overline{\Delta S}$. Using our baseline algorithm optimized via GHOSTS, we find that none of the host–SN combinations or NGC 4258 fields fall into the outlier category with this definition; however, we will make use of this form of outlier rejection when we consider variants of the CATS algorithm in Section 4. For our baseline analysis, we measure $\overline{\Delta S} = 15.213 \pm 0.049$ mag (i.e., the fiducial SN Ia is that many magnitudes brighter than the fiducial TRGB).

The combination of Equations (3) and (4) (i.e., rungs 1 and 2) provides the luminosity calibration of standardized SNe Ia,

$$M_B^0 = M_{I,\mathrm{TRGB}}^{R=4} - \overline{\Delta S}, \qquad (5)$$

from which we obtain $M_B^0 = -19.245 \pm 0.060$ mag. This quantity is directly comparable to $M_B^0 = -19.269$ from the SH0ES measurement using Cepheids in NGC 4258 (as the only anchor) and 42 SNe Ia in 37 Cepheid SN hosts (R22). These values are in excellent agreement, with a difference of 0.024 mag; the independent uncertainties (excluding SNe in common) add up in quadrature to an uncertainty of ~ 0.050 mag. The baseline SH0ES result using three independent geometric anchors is $M_B^0 = -19.253 \pm 0.027$, which is also very close to the TRGB result.

3.2.3. Third Rung

The third rung of the distance ladder is derived from SNe Ia only and is thus separable from any TRGB measurements. It can be summarized by the intercept of the Hubble diagram, $a_B = \log cz - 0.2 m_B^0$ in the low-redshift limit ($z \approx 0$), where z is the redshift, after correction for peculiar velocities (Carr et al. 2022; Peterson et al. 2022). Here m_B^0 is the maximum-light apparent magnitude of the SNe, which has been standardized (i.e., corrected for variations around the fiducial color, luminosity, and any host dependence following Pantheon+). For an arbitrary expansion history, a_B is expressed at small redshift by

$$a_B = \log cz \left\{ 1 + \frac{1}{2}[1 - q_0]z \right.$$
$$\left. - \frac{1}{6}[1 - q_0 - 3q_0^2 + j_0]z^2 + O(z^3) \right\} - 0.2 m_B^0. \qquad (6)$$

Here q_0 is the deceleration parameter, and j_0 is the jerk parameter (see Visser 2004, for definitions). We use a value of

$$a_B = 0.71448 \pm 0.0012 \qquad (7)$$

derived in R22 (and $q_0 = -0.55$ and $j_0 = 1$) for "all host types" at $0.0233 < z < 0.15$ from 484 SNe Ia, appropriate for a TRGB sample that includes early-type hosts (e.g., NGC 1404 and NGC 1316). We discuss this value further in Section 5.

We note that different surveys providing SN Ia magnitudes may yield different results for individual SNe, but these differences largely cancel, provided that the sample of m_B^0 is consistently calibrated using an all-sky survey (Brout et al. 2022a), and SNe from these same surveys are also used to measure the Hubble intercept, a_B (Brownsberger et al. 2023).

3.2.4. Baseline H_0

Combining the constraints from all three rungs, the Hubble constant H_0 is determined as

$$\log H_0 = 0.2 M_B^0 + a_B + 5, \qquad (8)$$

from which we find $H_0 = 73.22 \pm 2.06$ km s^{-1} Mpc^{-1}.

The uncertainty (in magnitudes) in the above follows from the quadrature sum of the above errors in μ_{N4258}, $m_{I,N4258,\mathrm{TRGB}}^{R=4}$, $\overline{dS}$, and $5a_B$:

$$\sigma_{top} = \frac{\sqrt{\sigma_{\mu_{0,N4258}}^2 + \sigma_{m_{N4258}^R}^2 + \sigma_{\Delta S}^2 + \sigma_{5a_B}^2}}{2.17} \times H_0. \qquad (9)$$

In magnitudes (km s^{-1} Mpc^{-1}), we find that the contributions from the four terms are 0.032 mag (1.1 km s^{-1} Mpc^{-1}), 0.014 mag (0.5 km s^{-1} Mpc^{-1}), 0.050 mag (1.7 km s^{-1} Mpc^{-1}), and 0.006 mag (0.2 km s^{-1} Mpc^{-1}), respectively. The quadrature sum is 0.061 mag or 2.8% or 2.06 km s^{-1} Mpc^{-1}.

These results represent the application of the TRGB algorithm as optimized to produce the lowest interhost variance of the tip for the GHOSTS training sample. However, there are uncertainties in the algorithm parameters that are difficult to propagate in any analytical form. Therefore, in the next section, we consider variants of the algorithm parameters from which we can determine other representative values of H_0 and an algorithmic systematic uncertainty.

4. Variants of TRGB Measurement Algorithm

4.1. Changing Algorithm Parameters

In Section 2.1, we described four features of a general TRGB measurement algorithm, each controlled by a parameter, and we determined the preferred parameter values as those that produce the lowest dispersion among the field tips measured around halos of the same hosts using the GHOSTS sample (W23) with a distance range of 2–15 Mpc (and which included one of the SN hosts studied here, NGC 7814). Because of the overlap in distances and contrast ratios between the GHOSTS sample and the SN hosts and fields in NGC 4258, we expect those choices to be appropriate for our present analysis. However, in order to understand the sensitivity of our results to those parameter choices, here we consider a wide range of variations that bracket their baseline values and thus estimate a systematic uncertainty in the determination of H_0 due to algorithm choices.

These variants are as follows.

1. *SpatialClip%* is varied from the nominal value of $>10\%$ with values of $>5\%$, $>10\%$, and $>20\%$.
2. The *Width* of the color band for the CMD is varied from the nominal at 1.0 mag to 0.75, 1.0, 1.5, and 2.0 mag. Here we included a fourth very large (near limitless) width to produce a more relevant comparison with the CCHP analysis in F19 for which little to no limitation in width was applied (T. Hoyt 2023, private communication).
3. The *Smooth σ* of the luminosity function is varied around the nominal of $\sigma = 0.1$ with three options, namely, $\sigma = 0.07$, 0.1, and 0.15.
4. *MinTh%* is varied from the nominal value of $0.6\times$ the highest EDR value with values of 0.5, 0.6, and 0.8.
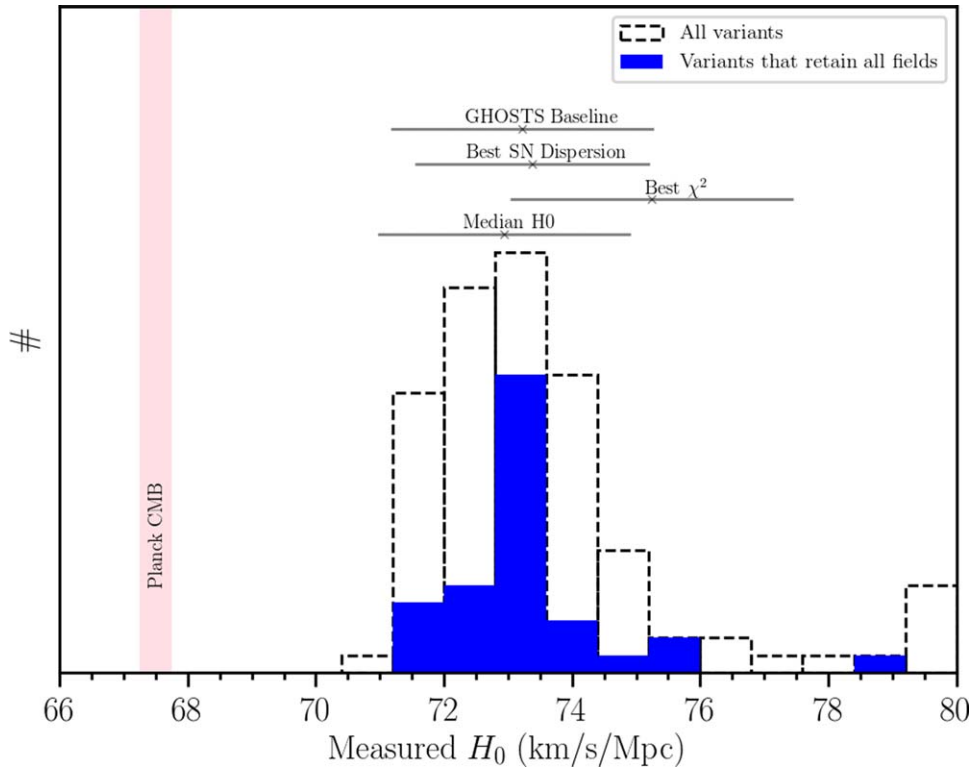
Figure 4. Distribution of recovered H_0 values for the variants described in Section 4.1. The values for the full set of 108 variants are shown by the black outline. The filled blue histogram shows only the variants in which tip measurements of all SN and NGC 4258 fields are recovered. We show the constraint on H_0 from Planck as well (pink). The horizontal lines around $H_0 = 73$ show the values recovered in Table 3.

The above choices provide a total of $3 \times 4 \times 3 \times 3 = 108$ variations on the analysis. We can characterize the variation in H_0 they produce in order to determine a systematic uncertainty relating to the TRGB algorithm. The variants also may be considered with appropriate context to identify some interesting and perhaps representative determinations of H_0, such as the median of all variants, the variant with the lowest χ^2 or dispersion, or the variant most similar to some literature analyses.

We summarize each variant in a table in the Appendix A, with the first four columns describing the analysis parameters, followed by the determination H_0, its error, the values of the first- and second-rung parameters, the total reduced χ^2 of the first and second rungs, the dispersion σ in the second rung, the number of TRGB tips found for the SN hosts, the number of SN hosts with a valid tip (a possible maximum of 13), and the total number of SNe contained in these hosts (a possible maximum of 18). We show the distribution of the measurements of H_0 in Figure 4. The formal dispersion of all variants is 2.94 km s^{-1} Mpc^{-1}, which exceeds the statistical error of 2.05 km s^{-1} Mpc^{-1}. There is a tighter core of values and a long, low tail toward high H_0 values. While our baseline measurement found no outliers among the SN or NGC 4258 fields, for a minority of variants, one or more fields are excluded as $>3\sigma$ outliers. To better understand how much of the variation in H_0 is due to the variation in the algorithm, we limit consideration of the variants to those that retain all SN hosts and NGC 4258 fields, some 55% of the variants. Doing so also largely eliminates the high H_0 tail as seen in Figure 4, and the remaining 59 variants have a median of 72.94 ± 1.98 km s^{-1} Mpc^{-1} and a standard deviation of ~ 1.33 km s^{-1} Mpc^{-1}. We consider this spread a fairer

representation of the systematic uncertainty due to the analysis process, as it does not include variations due to the exclusion of some data points. The full range of these variants is 71.2–78.4.

To further study the high H_0 tail seen in Figure 4, we show in Figure 5 that the source of the high H_0 tail can be seen as arising from variants that produce excess, i.e., "spurious," tips. Ideally, each host should have one TRGB. In practice, application of the EDR to hosts with a combination of poor contrast (low R), significant photometry noise, and a finite number of stars can in some cases produce multiple local maxima, all of which apply here. This consequence appears unavoidable. Following the approach we defined in W23, we retain multiple peaks, weight them by a function of their contrast ratio, and subject them to formal outlier clipping.

Similar to what was seen in W23, for variants where the number of tips per field approaches unity (<1.4), the results become more stable. The variants with a large ratio of tips per field tend to be those with lower smoothing, higher spatial clipping, and a lower minimum threshold. Overall, 66–108 variants have fewer than 1.4 tips per host, and 42 have more. We find that the largest driver for these is smoothing; the mean smoothing for variants with a tip-to-field ratio of <1.4 is 0.125, while it is 0.078 for variants with a tip-to-field ratio of >1.4. Interestingly, the smallest scatter for NGC 4258 is found with less smoothing; for smoothing of 0.07, 0.10, and 0.15 mag, the dispersion in tip magnitude is 0.047, 0.055, and 0.054 mag, respectively, including a lowest scatter of 0.027 mag for the case with 0.07 mag smoothing, 2.0 mag color width, and a 20% spatial clipping threshold. It is also worth noting that the high H_0 tail is supported by variants with less spatial clipping (the $>20\%$ threshold) with a modest correlation between H_0 and the level of spatial clipping, as seen in Figure 4.
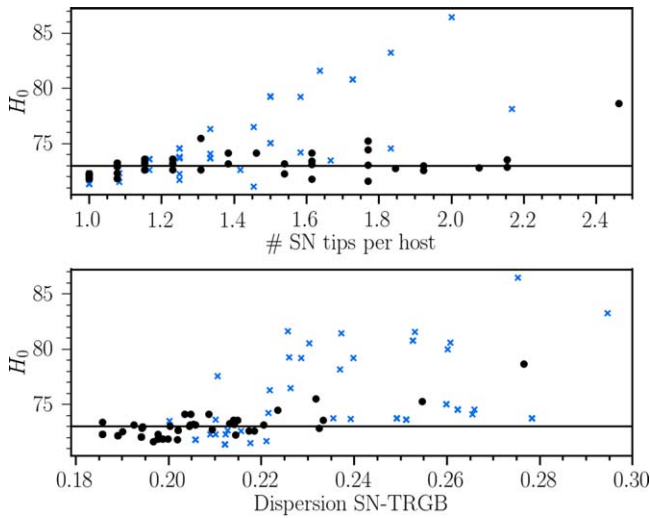
Figure 5. Inferred value of H_0 for all of the analysis variants as a function of the average number of tips per host (top) and the dispersion of the difference between SN and TRGB distances (bottom). Horizontal lines are drawn at $H_0 = 73$.

In Figure 6, we examine the impact of the different analysis parameters on H_0. The only obvious pull can be seen for the spatial clipping percentages, where the mean H_0 of the 5% distribution is ~ 0.7 km s^{-1} Mpc^{-1} lower than that for 10% or 20%. This can be traced to two fields of NGC 4258 where the more aggressive spatial clipping of 5% shifts the inferred tip value ~ 0.05 brighter. Some of the other variations in H_0 seen in Figure 6 can be traced to σ clipping. The most common SN field to be 3σ clipped from the SN host sample is NGC 4038, which is eliminated in 40 of 108 variants, a likely consequence of its greatest distance and fuzzy, ambiguous EDR with the two strongest and most distinct peaks. Object NGC 4526 fails in 13 of 108 variants. The other fields rarely fall out.

Based on the variants, we can define additional results of interest by "reoptimizing" the algorithm parameters with different parameter values, aiming to produce either the lowest dispersion between the SNe and tips or the lowest χ^2 overall. Doing so, these variants give 73.39 ± 1.83 km s^{-1} Mpc^{-1} with $\sigma = 0.18$ mag and 75.24 ± 2.21 km s^{-1} Mpc^{-1} with $\chi^2_{\rm dof} = 1.00$, respectively. We summarize these results as "Best SN dispersion" and "Best χ^2," respectively, in Table 3.

Finally, we consider one alternative to the analysis of fixing the center of the band to measure the TRGB. There is a range of ~ 0.4 mag in color exhibited by the fields analyzed, and the color is expected to vary as a function of age and metallicity (Salaris & Cassisi 1997; Bellazzini et al. 2001). Therefore, for GHOSTS, we have allowed the center of the band to float in order to maximize the number of stars in the band. If we fix the center to the median across all fields, we find that the values of H_0 as shown in Table 3 all shift by ~ 0.8 km s^{-1} Mpc^{-1} to higher values of H_0. We trace this pull to $\sim$three fields of NGC 4258 where the stellar locus appears more outside of the band in this case. We note that further analysis with a fixed center would likely require a new optimization of the other parameters as part of the CATS algorithm.

4.2. Effect of Tip-contrast Standardization on H_0

In this subsection, we consider the impact of ignoring the contrast ratio in our TRGB measurements: thus not using the

contrast ratio to inform the uncertainties of the tip measurements, and no standardization of the tip brightness. Determining these numbers facilitates comparison to literature studies. We summarize the possible results when neglecting tip standardization in Table 4.

To first approximation, the impact of the tip-magnitude and contrast relation on H_0 results from the difference in the mean contrast, R, for fields around NGC 4258 and SN hosts. We measure a weighted mean R (using Equation (2) as the weights) for NGC 4258 of 7.2 and the SN hosts of 5.2. This $\Delta R \sim 2$, based on Equation (1), biases the luminosity calibration of SNe from NGC 4258 by $0.021 \times 2 = 0.042$ mag, which is roughly 1.6 units in H_0. The simple average values of R (i.e., unweighted) are smaller at 6.6 and 4.6, respectively, but they have the same difference. Hence, we might expect H_0 to be $73-1.6 \sim 71.4$ by ignoring the tip-contrast relation (i.e., TCR $= 0$) or an equivalent method of tip standardization. However, in practice, estimating H_0 without use of the contrast ratio is more complex due to its role in distinguishing between low- and high-quality peaks in the same field.

The use of the contrast ratio, R, in W23 helped solve the common ambiguity of more than one strong peak in the EDR function used to locate the TRGB. As seen in Equation (2), the dependence of the tip uncertainty on R is quite steep, so this formula effectively selects the higher R tip by giving it far greater weight. For example, the two tips seen in Table 1 in NGC 1404 have $R = 6.9$ and 4.0, producing a 25-to-1 weighting. Without the use of the TCR and R weighting, we need to define a universal algorithm to measure the TRGB in the presence of multiple tips.

We tried several approaches, including selecting the highest peak in the EDR (called the "highest EDR peak") or the peak with the highest value of R (called the "highest R peak") when there is more than one in a field. Alternatively, we can take a straight average of the tips of multiple peaks (called the "average of peaks"). Lastly, there are a number of algorithmic variants that only produce a single peak for each field (called "one-tip variants"); for example, using a high smoothing value, $s = 0.15$, acts to merge smaller peaks into one. We summarize the results of all of these options in Table 4. Methods that favor the highest EDR peak (by smoothing or selecting) yield $H_0 \sim 71.7$, consistent with the first approximation of ignoring the TCR and the use of R to select the TRGB. Averaging multiple peaks or selecting the one with the highest R results in $H_0 \sim 75$. We conclude that there is a rather large ambiguity in H_0 related to the issue of selecting the tip among multiple peaks without the use of a strong, quantitative metric like R that can be applied uniformly.

The closest match of our algorithm to the CCHP analysis (Freedman et al. 2019) is to neglect the contrast ratio (including the TCR standardization) and select a variant with the highest color width, 2.0, while retaining all SN hosts. There are only six variants that satisfy all of these conditions, and they have a mean $H_0 = 71.8$ km s^{-1} Mpc^{-1}. As we show in Section 5, the larger share of the difference in H_0 between Freedman et al. (2019) and this work is not related to the TRGB measurement but rather to the treatment of the SN Ia sample.

5. Discussion: Comparison to Previous Constraints on H_0 with the TRGB

There have been four recent determinations of H_0 based on the TRGB and SNe that have substantial overlap of the sample
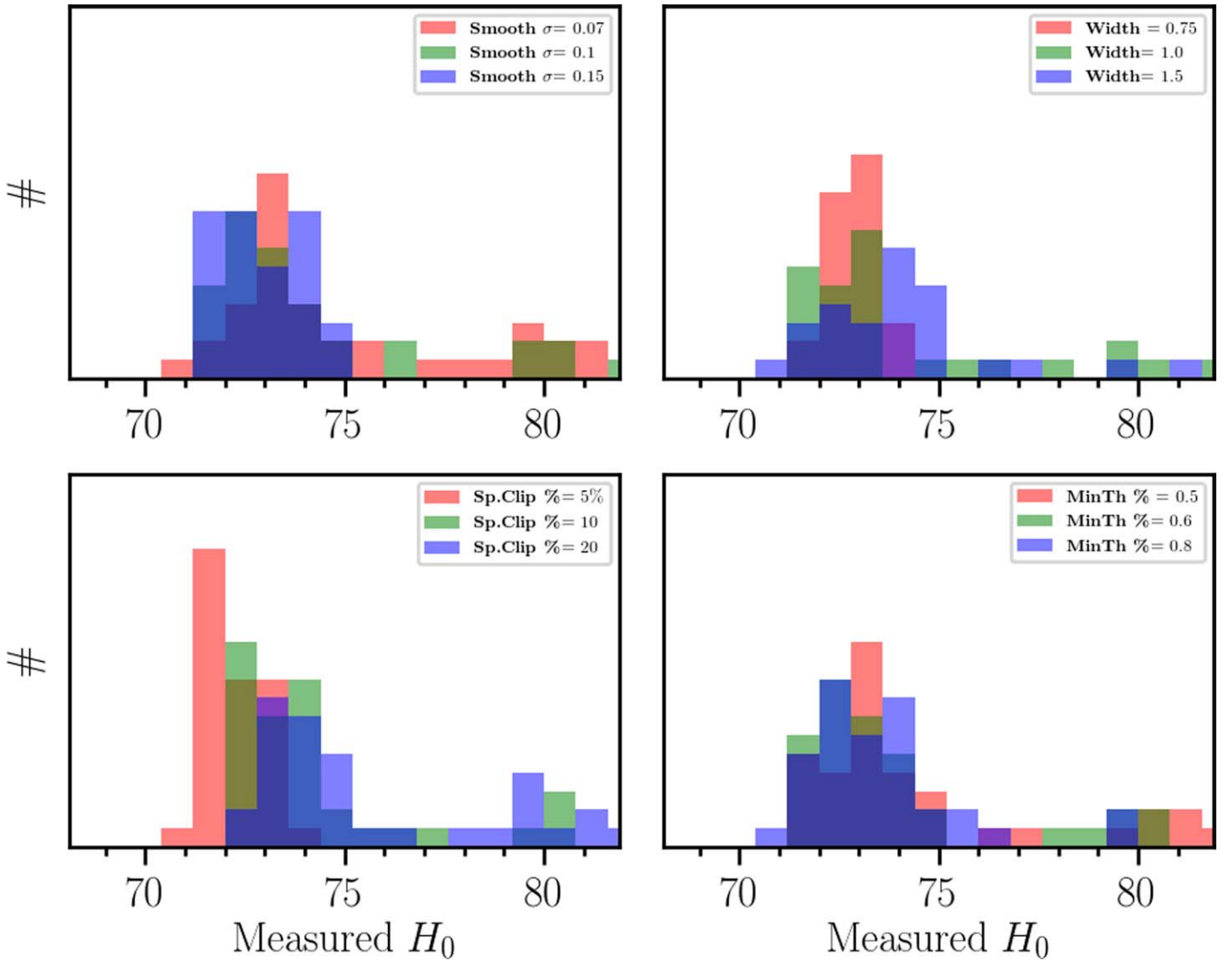
Figure 6. Impact of different variants in the analysis, summarizing the output of Table 6. (Top left) Recovered values of H_0 for all variants, broken into subsets according to the smoothing values used. (Top right) Same but broken into subsets using the widths of the color bands. (Bottom left) Same but broken into subsets using the fraction of the field clipped spatially. (Bottom right) Same but broken into categories varying the minimum threshold.

of host galaxies we used: the CCHP team measured $69.8 \pm 1.9 \text{ km s}^{-1} \text{Mpc}^{-1}$ (Freedman et al. 2019), the EDD group (which used luminosity function fitting rather than EDR to measure the TRGB) found $71.5 \pm 1.8 \text{ km s}^{-1} \text{Mpc}^{-1}$ (Anand et al. 2022), the RAISINs Team (Jones et al. 2022) used near-IR SN data (rather than optical) with the CCHP tip measurements and recovered $H_0 = 76.6 \pm 2.6 \text{ km s}^{-1} \text{Mpc}^{-1}$, and Dhawan et al. (2022) used only ZTF SN data and the CCHP tip method with a single TRGB host and measured $76.9 \pm 6.4 \text{ km s}^{-1} \text{Mpc}^{-1}$. Here we trace the differences between the results presented in this paper and these. The differences related to the first two are itemized in Table 5.

5.1. Differences in H_0 Due to the SN Data Analysis Component

Anand et al. (2022) used the Pantheon sample of SNe (Scolnic et al. 2018), a beta version of the Pantheon+ sample used here and consistent within $0.5 \text{ km s}^{-1} \text{Mpc}^{-1}$ for application to H_0 measurements (Brout et al. 2022c). Freedman et al. (2019) performed their own analysis of SNe and used a literature compilation for SNe in the calibrator hosts and the

CSP SN sample (Krisciunas et al. 2017) for the Hubble flow sample. As discussed in Brownsberger et al. (2023) and Brout et al. (2022b), use of different sources of SNe in the first and second rungs can lead to biases in the inferred value of H_0 due to SN calibration differences. Furthermore, unlike the analysis in Pantheon+ or the JLA compilation (Betoule et al. 2014), Freedman et al. (2019) did not apply peculiar velocity corrections to the Hubble flow sample, although the evidence of their value is $>4\sigma$ (Peterson et al. 2022).

To estimate the impact of these SN-related differences, we modify the Pantheon+ analysis in Brout et al. (2022b) and Riess et al. (2022). If we only include CSP Hubble flow data to measure the intercept of the third rung of the distance ladder, rather than all of the surveys contained in the Pantheon+ compilation, we measure a shift toward lower H_0 of $1.1 \text{ km s}^{-1} \text{Mpc}^{-1}$. This is consistent with the finding of Brout et al. (2022b; see Figure 6) of a 0.03 ± 0.015 mag difference between the CSP survey and the mean of all SN sources. Although this offset is not significant, it will nevertheless produce a difference of $1 \text{ km s}^{-1} \text{Mpc}^{-1}$ if it is the sole source

Table 3
Baseline and Representative Results on H_0

Method	H_0	$m_{I,N4258,TRGB}^{R=4}$	$\overline{\Delta S}$
GHOSTS baseline	73.22 ± 2.06 km s^{-1} Mpc^{-1}	25.361 ± 0.0136	15.213 ± 0.049
Best SN dispersion	73.39 ± 1.83 km s^{-1} Mpc^{-1}	25.355 ± 0.015	15.201 ± 0.040
Best χ^2	75.24 ± 2.21 km s^{-1} Mpc^{-1}	25.374 ± 0.015	15.164 ± 0.052
Median H_0	72.94 ± 1.98 km s^{-1} Mpc^{-1}	25.353 ± 0.014	15.213 ± 0.046

Note. Recovered values for specific variant cases that produce optimal results. The derivations for H_0, $m_{I,N4258,TRGB}^{R=4}$, and $\overline{\Delta S}$ are given in Equations (8), (3), and (4), respectively. The results are discussed in Section 4.1. Each variant includes all SN and NGC 4258 fields with tip measurements.

Table 4
Neglecting Tip Standardization: Dependence on Method for Selecting Tips

Method	H_0	$m_{I,N4258,TRGB}$	$\overline{\Delta S}$
Highest EDR peak	71.7 ± 2.6	25.30 ± 0.05	15.20 ± 0.05
Highest R peak	74.1 ± 2.7	25.30 ± 0.05	15.12 ± 0.05
Average of peaks	75.3 ± 2.5	25.38 ± 0.04	15.15 ± 0.05
One-tip variants	71.7 ± 2.6	25.30 ± 0.05	15.20 ± 0.05

Note. Results of various methods when ignoring the use of R to standardize tips. Each is discussed in Section 4.2.

Table 5
Sources of Differences in H_0 between TRGB Analysis by CATS (Here), CCHP, and EDD (in H_0)

Term	ΔCCHP (km s^{-1} Mpc^{-1})	ΔEDD (km s^{-1} Mpc^{-1})
SN-related		
(1) Include SNe 2021pit, 2021rhu, 2007on	0.6	1.3
(2) No TRGB detected in N5584, N3021, N1309, N3370	0.0	0.0
(3) Peculiar flows (Pantheon+)	0.4	0.0
(4) Hubble flow surveys (Pantheon+)	1.1	0.0
SN subtotal	2.0	1.3
TRGB-related		
(5) Fiducial TRGB calibration/tip-contrast relation	1.4	-0.3
Total	3.4	1.0

Note. ΔCCHP = differences from Freedman (2021) and EDD = differences from Anand et al. (2022). Descriptions of individual entries: (1) CCHP did not include the two SNe from 2021 and excluded SN 2007on, and EDD did not include the two from 2021. (2) Neither CATS nor EDD detected the TRGB in these four most distant SN host galaxies. (3) Pantheon+ accounts for peculiar motions that produce a highly significant improvement in the dispersion of the Hubble diagram (see Peterson et al. 2022). (4) CCHP measures the Hubble flow from a single SN survey that has an offset with respect to the mean of many surveys in Pantheon+, as shown in Brownsberger et al. (2023). (5) This term is the difference in the calibration of TRGB from NGC 4258 as applied to SN hosts and is discussed in Section 4.

used to measure the Hubble flow in relation to the second rung, which uses all samples.

In addition, if we remove the peculiar velocity correction (for the CSP sample), this shifts the inferred H_0 lower by ~ 0.4 km s^{-1} Mpc^{-1}, consistent with the findings of Peterson et al. (2022). This amount is somewhat smaller than that found for the full sample in Peterson et al. (2022) of ~ 0.6–0.7 km s^{-1} Mpc^{-1} because of the location of the CSP SNe in

the sky and the redshift range of the SNe ($0.02 < 0.15$) used to measure H_0. Combined, these two distinct effects contribute a shift of 1.5 km s^{-1} Mpc^{-1} toward a lower H_0 relative to Freedman et al. (2019). They do not produce any difference from any of the three other studies; EDD (Anand et al. 2022) and ZTF (Dhawan et al. 2022) use flow corrections and matched surveys, while RAISINs (Jones et al. 2022) uses only CSP SNe but on both rungs of the distance ladder. These factors partially explain why these other analyses all yield higher values of H_0.

Additionally, we include two new calibrator SNe Ia from 2021, SN 2021rhu from Dhawan et al. (2022) and SN 2021pit (Brown et al. 2014; in NGC 1448, which already included SN 2001el). We also include SN 2007on, used by Freedman et al. (2019) but excluded by Freedman (2021). The combined impact of the additional three SNe Ia is 0.6 km s^{-1} Mpc^{-1} relative to Freedman (2021). The EDD already included 2007on but did not include the 2021 SNe, so the relative change from the two additional SNe is 1.3 km s^{-1} Mpc^{-1}.

The four hosts for which neither we nor EDD could detect a reliable tip, i.e., NGC 5584, 3021, 3370, and 1309, as evaluated by reanalyzing the CCHP result with and without them, cause no change in H_0 when they are excluded from a reanalysis of the CCHP results, although the uncertainty increases by 10%.

These effects combined account for a net difference of 2.0 km s^{-1} Mpc^{-1} between this study and the CCHP for SNe-related terms that are independent of the TRGB. Simply revising the SN data in Freedman et al. (2019) with Pantheon+ would yield an H_0 of 71.8 km s^{-1} Mpc^{-1}, which well matches the value we found for the TRGB algorithm variants that most closely match the CCHP procedures. For EDD, the only difference is the two new SNe from 2021, which cause a change of 1.3 km s^{-1} Mpc^{-1}, and revising the EDD analysis with the new objects would yield an H_0 of 72.8 km s^{-1} Mpc^{-1}. Such changes due to a couple of new SNe is not surprising given the still small number of SNe in well-measured TRGB hosts.

5.2. Differences in H_0 Due to the TRGB Data Analysis Component

The remaining differences between our analysis and those of Anand et al. (2022) and Freedman et al. (2019) relate to the fiducial calibration of the TRGB derived from NGC 4258 and applied to SN hosts. As discussed in Section 4, there is a difference in the mean tip contrast between the fields of NGC 4258 and SN hosts of $\Delta R \sim 2$, which, via the tip contrast relation of 0.021 mag per unit in R, produces a difference of $+1.6$ km s^{-1} Mpc^{-1} with this analysis and that from CCHP, though there is a difference of -0.3 km s^{-1} Mpc^{-1} from EDD due to the specific fields used in that analysis.

A direct way to understand the difference in H_0 derived here versus that derived in CCHP or EDD is by comparing the magnitude of the tip in NGC 4258 estimated by each group. Including removal of MW extinction (and excluding removal of extinction in NGC 4258 for even comparison), the value found here "corrected to the mean R of the SN hosts" is 25.389 ± 0.00136. Our simple mean of the NGC 4258 fields (i.e., without use of the contrast ratio) is 25.371 ± 0.041 (or 25.44 when weighting the tip by the number of stars below the tip). Jang (2023) found 25.347 ± 0.015 (after MW extinction removal) from the outer region of a field overlapping field 3 from L23, which would propagate to the ΔH_0 of 1.6 stated above with CCHP. On the other hand, EDD finds 25.402 ± 0.025 from a combination of different fields, 5 and 6 from L23, though EDD applies a color correction that lowers the luminosity of the tip by ~ 0.02 mag so that the difference in calibration with this study and EDD is -0.3 km s^{-1} Mpc^{-1}. Without standardization, the differences seen in the tip around NGC 4258 may be subject to the vagaries of individual field properties. Specifically selecting the highest-contrast (i.e., brightest) fields in NGC 4258 without a similar selection in the SN fields would lead to a bias in H_0.

More challenging is the ambiguity related to EDR tip selection. As discussed in Section 4.2, there are several reasonable ways to identify the tip for a lumpy EDR of distant galaxies; as we report in Table 4, these can change H_0 by up to 5 km s^{-1} Mpc^{-1} (e.g., between straight averaging peaks versus highest EDR peak) if the tips are not standardized and subjected to quality criteria to determine their individual precisions. It is important to define an algorithm for doing this a priori to avoid the potential for bias that may result from a case-by-case treatment. Absent an unsupervised algorithm, a low dispersion between SNe Ia and the TRGB could result from utilizing additional information in the CMD or by selecting the best tip with some dependence of the knowledge of the SN brightness. As a result, such low dispersion without an algorithmic approach may be unrealistic or at least not an independent measure of TRGB precision.

We note that we directly use the photometry from Anand et al. (2022), but we expect that the photometry from Freedman et al. (2019), if available, would be similar (as discussed in Jang 2023). Finally, we remark that a central finding for this analysis and the preceding one from W23 is that the TRGB from edge detection must be treated as a standardizable, rather than standard, candle. A recent study by Anderson et al. (2023) reinforced this viewpoint by measuring at 5σ two subpopulations of RGB stars based on their variability. Remeasuring the absolute brightness of the TRGB from the LMC but keeping the rest of the CCHP analysis, they found a higher value of H_0 of 71.8 ± 1.5 km s^{-1} Mpc^{-1}, which is similar to our finding after excluding SN-related differences. These works indicate that the TRGB measured from EDR should not be assumed to be a standard candle (or unbiased by the measurement process) but rather can and should be standardized using empirical measures calibrated from a large set of fields around the same host.

6. Conclusions

This analysis applies a standardized TRGB relation over a narrow color range to constrain H_0. We find a value of $H_0 = 73.22 \pm 2.06$ km s^{-1} Mpc^{-1} for our nominal analysis, with a standard deviation of the variants of the analysis of ~ 1 km s^{-1} Mpc^{-1}. We quantify that the application of the TCR relation increases the inferred value of H_0 by ~ 1.4 km s^{-1} Mpc^{-1} compared to previous studies while also providing a robust methodology for dealing with multiple tip detections for fields. We find that a larger difference compared to previous TRGB studies is due to the SN component of the analysis; using the recent Pantheon+ data set increases H_0 by ~ 2.0 km s^{-1} Mpc^{-1}. Our results address what is arguably the most pressing challenge to the validity of the Hubble tension, in that some previous TRGB results appeared to straddle the range between late- and early-Universe measurements of H_0. This result further clarifies this tension as one of the most pressing problems in cosmology today.

Data Availability

We include all of the data and code used for this analysis. Photometry for the SN hosts and NGC 4258 is based on the EDD CMDs/TRGB catalog (Tully et al. 2009; Anand et al. 2021a) pipeline and is accessible at https://edd.ifa.hawaii.edu. The training data come from the GHOSTS program (Radburn-Smith et al. 2011) and are accessible at https://archive.stsci.edu/prepds/ghosts/ghosts/survey.html. For ease, we also rerelease these data along with our codes at https://github.com/JiaxiWu1018/CATS-H0.

Facilities: MAST, HST:ACS.

Software: Astropy (Astropy Collaboration et al. 2013, 2018), Matplotlib (Hunter 2007), NumPy (van der Walt et al. 2011; Harris et al. 2020).

Appendix A
Data Table for Impact of Variants

We present all of the variants considered in this analysis in Table 6. As discussed in Section 4.1, we have four separate variant parameters. For each run, we report the values of the variant parameters (columns (1)–(4)). We then report the inferred value of H_0 and its statistical uncertainty (column (5)), the mean value of the brightness difference between the SN magnitudes and TRGB brightnesses (column (6)), the mean value of the brightness difference between the TRGB brightnesses of NGC 4258 and the geometric distance measurement (column (7)), the χ^2/N of the residuals of the SN-TRGB rung (column (8)), the dispersion of the residuals in the SN-TRGB rung (column (9)), the number of TRGB tips of SN hosts measured (column (10)), the number of SN hosts with a tip measured (column (11)), and the number of SNe in those hosts (column (12)).

Table 6
Analysis Variants and Their Impact on Recovered Parameters

| Sp.Clip% (1)	Width (2)	Smooth σ (3)	MinTh% (4)	H_0 (5)	$\overline{\Delta S}$ (6)	$m^{R=4}_{I,N4258,\mathrm{TRGB}}$ (7)	χ^2/N (8)	σ (9)	SN Tips (10)	SN Hosts (11)	SNe (12)
10%	0.75	0.07	0.5	71.93 ± 1.85	15.19 ± 0.04	25.30 ± 0.01	9.07	0.20	23	13	18
10%	0.75	0.07	0.6	72.48 ± 1.88	15.21 ± 0.04	25.33 ± 0.01	7.73	0.20	21	13	18
10%	0.75	0.07	0.8	74.02 ± 1.93	15.22 ± 0.04	25.39 ± 0.01	2.48	0.20	18	13	18
10%	0.75	0.10	0.5	72.74 ± 1.97	15.23 ± 0.05	25.37 ± 0.01	1.36	0.21	18	13	18
10%	0.75	0.10	0.6	72.74 ± 1.98	15.25 ± 0.05	25.39 ± 0.01	2.29	0.21	17	13	18
10%	0.75	0.10	0.8	72.76 ± 1.98	15.25 ± 0.05	25.39 ± 0.01	2.49	0.21	16	13	18
10%	0.75	0.15	0.5	71.80 ± 1.91	15.25 ± 0.04	25.35 ± 0.01	1.51	0.18	13	13	18
10%	0.75	0.15	0.6	71.81 ± 1.91	15.25 ± 0.04	25.35 ± 0.01	1.51	0.18	13	13	18
10%	0.75	0.15	0.8	71.81 ± 1.91	15.25 ± 0.04	25.35 ± 0.01	1.51	0.18	13	13	18
10%	1.0	0.07	0.5	71.74 ± 1.93	15.21 ± 0.05	25.32 ± 0.01	21.11	0.21	22	13	18
10%	1.0	0.07	0.6	71.83 ± 1.97	15.23 ± 0.05	25.34 ± 0.02	25.27	0.21	20	13	18
10%	1.0	0.07	0.8	75.55 ± 1.95	15.18 ± 0.04	25.39 ± 0.01	2.04	0.23	17	13	18
10%	1.0	0.10	0.5	73.10 ± 2.05	15.24 ± 0.05	25.38 ± 0.01	1.68	0.21	15	13	18
10%	1.0	0.10	0.6	73.02 ± 2.05	15.24 ± 0.05	25.38 ± 0.01	1.79	0.21	15	13	18
10%	1.0	0.10	0.8	72.34 ± 2.06	15.27 ± 0.05	25.39 ± 0.01	2.17	0.19	14	13	18
10%	1.0	0.15	0.5	71.85 ± 1.99	15.25 ± 0.05	25.36 ± 0.01	1.70	0.19	13	13	18
10%	1.0	0.15	0.6	71.87 ± 1.99	15.25 ± 0.05	25.36 ± 0.01	1.71	0.19	13	13	18
10%	1.0	0.15	0.8	71.87 ± 1.99	15.25 ± 0.05	25.36 ± 0.01	1.71	0.19	13	13	18
10%	1.5	0.07	0.5	75.89 ± 1.90	15.12 ± 0.04	25.35 ± 0.02	20.85	0.23	32	13	18
10%	1.5	0.07	0.6	73.71 ± 1.95	15.18 ± 0.04	25.35 ± 0.02	9.22	0.23	28	13	18
10%	1.5	0.07	0.8	72.96 ± 1.99	15.21 ± 0.05	25.35 ± 0.01	1.83	0.20	20	12	17
10%	1.5	0.10	0.5	73.90 ± 2.15	15.21 ± 0.05	25.38 ± 0.01	1.55	0.23	17	12	17
10%	1.5	0.10	0.6	73.58 ± 2.17	15.22 ± 0.05	25.38 ± 0.01	1.55	0.24	16	12	17
10%	1.5	0.10	0.8	71.77 ± 2.14	15.24 ± 0.05	25.35 ± 0.01	1.87	0.21	14	12	17
10%	1.5	0.15	0.5	72.77 ± 2.10	15.19 ± 0.05	25.33 ± 0.01	1.53	0.25	14	12	17
10%	1.5	0.15	0.6	72.77 ± 2.10	15.19 ± 0.05	25.33 ± 0.01	1.53	0.25	14	12	17
10%	1.5	0.15	0.8	72.77 ± 2.10	15.19 ± 0.05	25.33 ± 0.01	1.53	0.25	14	12	17
10%	2.0	0.07	0.5	80.33 ± 2.25	15.03 ± 0.05	25.38 ± 0.02	5.95	0.25	31	11	16
10%	2.0	0.07	0.6	80.93 ± 2.27	15.03 ± 0.05	25.39 ± 0.01	3.46	0.25	28	11	16
10%	2.0	0.07	0.8	74.30 ± 2.17	15.19 ± 0.05	25.37 ± 0.01	1.03	0.25	22	12	17
10%	2.0	0.10	0.5	81.00 ± 2.42	15.02 ± 0.05	25.39 ± 0.01	1.55	0.25	19	11	16
10%	2.0	0.10	0.6	81.00 ± 2.42	15.02 ± 0.05	25.39 ± 0.01	1.55	0.25	19	11	16
10%	2.0	0.10	0.8	73.78 ± 2.29	15.20 ± 0.06	25.37 ± 0.01	1.54	0.26	16	12	17
10%	2.0	0.15	0.5	73.26 ± 2.25	15.19 ± 0.06	25.34 ± 0.02	1.10	0.27	15	12	17
10%	2.0	0.15	0.6	73.46 ± 2.25	15.19 ± 0.06	25.34 ± 0.02	1.06	0.27	15	12	17
10%	2.0	0.15	0.8	73.46 ± 2.25	15.19 ± 0.06	25.34 ± 0.02	1.06	0.27	15	12	17
20%	0.75	0.07	0.5	71.15 ± 1.91	15.18 ± 0.04	25.26 ± 0.02	24.04	0.20	25	13	18
20%	0.75	0.07	0.6	73.38 ± 1.94	15.21 ± 0.04	25.36 ± 0.01	8.30	0.20	21	13	18
20%	0.75	0.07	0.8	74.11 ± 1.97	15.22 ± 0.05	25.39 ± 0.01	2.48	0.20	19	13	18
20%	0.75	0.10	0.5	72.67 ± 2.03	15.24 ± 0.05	25.37 ± 0.01	1.17	0.20	16	13	18
20%	0.75	0.10	0.6	72.15 ± 2.04	15.25 ± 0.05	25.37 ± 0.01	1.16	0.20	15	13	18
20%	0.75	0.10	0.8	72.41 ± 2.05	15.25 ± 0.05	25.38 ± 0.01	1.43	0.20	15	13	18
20%	0.75	0.15	0.5	72.92 ± 1.98	15.24 ± 0.05	25.38 ± 0.01	1.81	0.19	14	13	18
20%	0.75	0.15	0.6	72.92 ± 1.98	15.24 ± 0.05	25.38 ± 0.01	1.81	0.19	14	13	18
20%	0.75	0.15	0.8	72.92 ± 1.98	15.24 ± 0.05	25.38 ± 0.01	1.81	0.19	14	13	18
20%	1.0	0.07	0.5	79.79 ± 1.93	14.97 ± 0.04	25.31 ± 0.01	16.59	0.23	32	12	17
20%	1.0	0.07	0.6	79.79 ± 1.97	15.02 ± 0.04	25.35 ± 0.01	10.82	0.23	27	12	17
20%	1.0	0.07	0.8	76.28 ± 1.97	15.15 ± 0.04	25.39 ± 0.01	1.34	0.22	19	13	18
20%	1.0	0.10	0.5	82.84 ± 2.31	14.97 ± 0.05	25.39 ± 0.01	1.17	0.25	19	11	14
20%	1.0	0.10	0.6	80.09 ± 2.22	15.04 ± 0.05	25.38 ± 0.01	1.23	0.25	19	12	17
20%	1.0	0.10	0.8	74.01 ± 2.10	15.22 ± 0.05	25.39 ± 0.01	1.35	0.23	17	13	18
20%	1.0	0.15	0.5	73.24 ± 2.05	15.23 ± 0.05	25.37 ± 0.01	2.14	0.21	14	13	18
20%	1.0	0.15	0.6	73.24 ± 2.05	15.23 ± 0.05	25.37 ± 0.01	2.14	0.21	14	13	18
20%	1.0	0.15	0.8	73.24 ± 2.05	15.23 ± 0.05	25.37 ± 0.01	2.14	0.21	14	13	18
20%	1.5	0.07	0.5	81.10 ± 2	14.96 ± 0.04	25.33 ± 0.02	9.07	0.24	34	12	17
20%	1.5	0.07	0.6	73.90 ± 1.99	15.18 ± 0.04	25.35 ± 0.02	4.11	0.21	29	13	18
20%	1.5	0.07	0.8	73.26 ± 2.10	15.19 ± 0.05	25.34 ± 0.01	0.97	0.22	19	12	17
20%	1.5	0.10	0.5	74.59 ± 2.18	15.17 ± 0.05	25.36 ± 0.01	1.20	0.26	18	12	17
20%	1.5	0.10	0.6	74.67 ± 2.18	15.17 ± 0.05	25.36 ± 0.01	1.26	0.26	18	12	17
20%	1.5	0.10	0.8	72.54 ± 2.16	15.20 ± 0.05	25.33 ± 0.01	1.70	0.23	16	12	17
20%	1.5	0.15	0.5	73 ± 2.13	15.17 ± 0.05	25.32 ± 0.02	1.35	0.25	15	12	17
20%	1.5	0.15	0.6	73 ± 2.13	15.17 ± 0.05	25.32 ± 0.02	1.35	0.25	15	12	17
20%	1.5	0.15	0.8	73 ± 2.13	15.17 ± 0.05	25.32 ± 0.02	1.35	0.25	15	12	17

Table 6
(Continued)

Sp.Clip% (1)	Width (2)	Smooth σ (3)	MinTh% (4)	H_0 (5)	$\overline{\Delta S}$ (6)	$m_{I,N4258,TRGB}^{R=4}$ (7)	χ^2/N (8)	σ (9)	SN Tips (10)	SN Hosts (11)	SNe (12)
20%	2.0	0.07	0.5	81.05 ± 2.15	14.98 ± 0.04	25.35 ± 0.01	4.62	0.24	35	12	17
20%	2.0	0.07	0.6	78.24 ± 2.01	15.07 ± 0.04	25.36 ± 0.01	3.48	0.27	32	13	18
20%	2.0	0.07	0.8	76.12 ± 2.20	15.14 ± 0.05	25.37 ± 0.01	1.02	0.30	25	13	18
20%	2.0	0.10	0.5	86.22 ± 2.53	14.88 ± 0.05	25.38 ± 0.02	1.18	0.27	22	11	14
20%	2.0	0.10	0.6	83.13 ± 2.42	14.96 ± 0.05	25.38 ± 0.02	1.17	0.28	22	12	17
20%	2.0	0.10	0.8	74.78 ± 2.29	15.15 ± 0.06	25.34 ± 0.02	1.45	0.30	19	13	18
20%	2.0	0.15	0.5	73.30 ± 2.28	15.20 ± 0.06	25.35 ± 0.02	1.62	0.24	15	12	17
20%	2.0	0.15	0.6	73.03 ± 2.27	15.20 ± 0.06	25.34 ± 0.02	1.77	0.24	15	12	17
20%	2.0	0.15	0.8	73.03 ± 2.27	15.20 ± 0.06	25.34 ± 0.02	1.77	0.24	15	12	17
5%	0.75	0.07	0.5	70.38 ± 1.69	15.22 ± 0.04	25.28 ± 0.01	13.40	0.19	23	13	18
5%	0.75	0.07	0.6	70.78 ± 1.72	15.23 ± 0.04	25.31 ± 0.01	15.54	0.19	21	13	18
5%	0.75	0.07	0.8	72.70 ± 1.80	15.25 ± 0.04	25.38 ± 0.01	0.70	0.20	16	13	18
5%	0.75	0.10	0.5	72.72 ± 1.84	15.25 ± 0.04	25.39 ± 0.01	1.37	0.20	16	13	18
5%	0.75	0.10	0.6	72.77 ± 1.84	15.25 ± 0.04	25.39 ± 0.01	1.49	0.20	16	13	18
5%	0.75	0.10	0.8	73.17 ± 1.86	15.26 ± 0.04	25.41 ± 0.01	1.70	0.20	15	13	18
5%	0.75	0.15	0.5	71.67 ± 1.84	15.26 ± 0.04	25.36 ± 0.01	1.32	0.18	13	13	18
5%	0.75	0.15	0.6	71.67 ± 1.84	15.26 ± 0.04	25.36 ± 0.01	1.32	0.18	13	13	18
5%	0.75	0.15	0.8	71.93 ± 1.85	15.26 ± 0.04	25.37 ± 0.01	1.44	0.18	13	13	18
5%	1.0	0.07	0.5	72.61 ± 1.81	15.22 ± 0.04	25.35 ± 0.01	10.43	0.18	21	13	18
5%	1.0	0.07	0.6	73.35 ± 1.85	15.24 ± 0.04	25.40 ± 0.01	4.95	0.19	20	13	18
5%	1.0	0.07	0.8	73.46 ± 1.91	15.26 ± 0.04	25.41 ± 0.01	2.05	0.21	15	13	18
5%	1.0	0.10	0.5	71.64 ± 1.95	15.28 ± 0.05	25.38 ± 0.01	5.48	0.19	14	13	18
5%	1.0	0.10	0.6	71.74 ± 1.95	15.28 ± 0.05	25.38 ± 0.01	5.36	0.19	14	13	18
5%	1.0	0.10	0.8	71.72 ± 1.96	15.28 ± 0.05	25.38 ± 0.01	6.34	0.19	13	13	18
5%	1.0	0.15	0.5	71.53 ± 1.93	15.26 ± 0.05	25.35 ± 0.01	1.59	0.19	13	13	18
5%	1.0	0.15	0.6	71.53 ± 1.93	15.26 ± 0.05	25.35 ± 0.01	1.59	0.19	13	13	18
5%	1.0	0.15	0.8	71.53 ± 1.93	15.26 ± 0.05	25.35 ± 0.01	1.59	0.19	13	13	18
5%	1.5	0.07	0.5	73.07 ± 1.87	15.22 ± 0.04	25.36 ± 0.01	5.74	0.19	27	13	18
5%	1.5	0.07	0.6	73.08 ± 1.88	15.23 ± 0.04	25.37 ± 0.01	2.70	0.19	25	13	18
5%	1.5	0.07	0.8	67.91 ± 2.08	15.36 ± 0.06	25.35 ± 0.01	1.35	0.09	15	11	16
5%	1.5	0.10	0.5	73.68 ± 2.10	15.24 ± 0.05	25.40 ± 0.01	1.42	0.21	15	12	17
5%	1.5	0.10	0.6	72.05 ± 2.12	15.27 ± 0.05	25.39 ± 0.01	1.48	0.20	13	12	17
5%	1.5	0.10	0.8	71.06 ± 2.09	15.26 ± 0.05	25.34 ± 0.01	1.71	0.20	12	12	17
5%	1.5	0.15	0.5	70.53 ± 2.03	15.24 ± 0.05	25.31 ± 0.02	1.41	0.20	12	12	17
5%	1.5	0.15	0.6	70.53 ± 2.03	15.24 ± 0.05	25.31 ± 0.02	1.41	0.20	12	12	17
5%	1.5	0.15	0.8	70.53 ± 2.03	15.24 ± 0.05	25.31 ± 0.02	1.41	0.20	12	12	17
5%	2.0	0.07	0.5	75.85 ± 1.97	15.16 ± 0.04	25.38 ± 0.01	5.25	0.24	29	13	18
5%	2.0	0.07	0.6	75.89 ± 2	15.17 ± 0.04	25.40 ± 0.02	3.63	0.23	25	13	18
5%	2.0	0.07	0.8	71.64 ± 2.11	15.26 ± 0.05	25.36 ± 0.01	6.84	0.21	15	12	17
5%	2.0	0.10	0.5	72.83 ± 2.23	15.24 ± 0.06	25.37 ± 0.02	0.60	0.21	17	12	17
5%	2.0	0.10	0.6	71.92 ± 2.26	15.26 ± 0.06	25.37 ± 0.02	0.60	0.22	15	12	17
5%	2.0	0.10	0.8	70.52 ± 2.22	15.26 ± 0.06	25.32 ± 0.02	0.60	0.21	13	12	17
5%	2.0	0.15	0.5	70.25 ± 2.17	15.25 ± 0.06	25.31 ± 0.02	1.10	0.21	12	12	17
5%	2.0	0.15	0.6	70.19 ± 2.17	15.25 ± 0.06	25.31 ± 0.02	1.11	0.21	12	12	17
5%	2.0	0.15	0.8	70.19 ± 2.17	15.25 ± 0.06	25.31 ± 0.02	1.11	0.21	12	12	17

Appendix B
Four SN Ia Hosts that Lack a Significant Tip Detection

There are four galaxies, NGC 5584, 3021, 3370, and 1309, that are also the most distant of the sample, with expected 32 mag $< \mu <$ 32.7 mag based on their SNe Ia (and Cepheids), for which we do not detect a significant tip. The HST observations of these galaxies targeted the disk in order to measure Cepheid variables (R22), making it doubly difficult to measure their TRGBs. The TRGB measurements via edge detection were obtained by Jang et al. (2018), with tip magnitudes $m_I \sim 28$ and formal uncertainties of $\leqslant 0.1$ mag. These values were retained

in the analyses of Freedman et al. (2019) and Freedman (2021). Anand et al. (2022) remeasured the photometry for these hosts and determined that the CMDs were not deep enough to measure their TRGBs, with the expected location of the tip approaching S/N ~ 3, in good agreement with the HST exposure time calculator, so this conclusion is not sensitive to the method used to measure the photometry.

We show the CMDs for these galaxies in Figure 7. We fail to detect a significant tip in a broad 1 mag range centered on the expected value. A more rigorous metric, the value of R, never exceeds 2 across that interval (right side of each panel). Therefore, even if a tip was found in this range, the analysis in W23 has
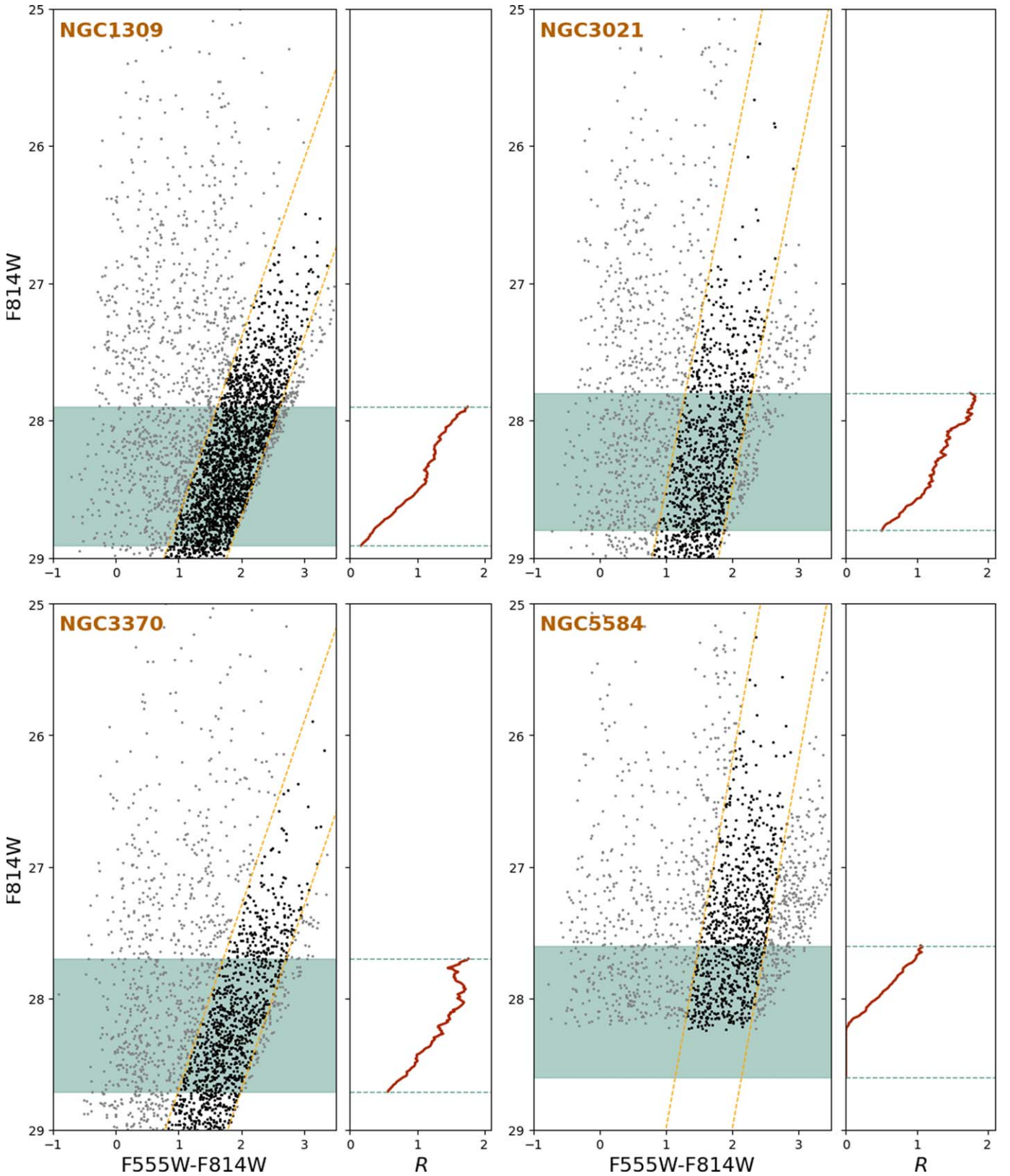
Figure 7. The CMDs and contrast ratio vs. F814W magnitude plots for NGC 1309, NGC 3021, NGC 3370, and NGC 5584. The shaded green region is the expected TRGB in the F814W filter as shown by the curve to the right of each CMD; the value of the contrast ratio R at those magnitudes never exceeds 2.

empirically demonstrated that the uncertainty of tips with such little contrast ($R < 2$) is >1 mag, making such a measurement meaningless. We therefore follow the decision of Anand et al. (2022) to remove these galaxies from our sample. It is incumbent

upon any future analysis that seeks to make use of TRGB measurements in these hosts to provide the data and tools necessary to demonstrate that these hosts yield a significant TRGB measurement.

ORCID iDs

D. Scolnic ⓘ https://orcid.org/0000-0002-4934-5849
A. G. Riess ⓘ https://orcid.org/0000-0002-6124-1196
J. Wu ⓘ https://orcid.org/0000-0003-3829-967X
S. Li ⓘ https://orcid.org/0000-0002-8623-1082
G. S. Anand ⓘ https://orcid.org/0000-0002-5259-2314
R. Beaton ⓘ https://orcid.org/0000-0002-1691-8217
R. I. Anderson ⓘ https://orcid.org/0000-0001-8089-4419
S. Dhawan ⓘ https://orcid.org/0000-0002-2376-6979

References

Ahumada, R., Allende Prieto, C., Almeida, A., et al. 2020, ApJS, 249, 3
Anand, G. S., Lee, J. C., Van Dyk, S. D., et al. 2021b, MNRAS, 501, 3621
Anand, G. S., Rizzi, L., Tully, R. B., et al. 2021a, AJ, 162, 80
Anand, G. S., Tully, R. B., Rizzi, L., Riess, A. G., & Yuan, W. 2022, ApJ, 932, 15
Anderson, R. I. 2022, A&A, 658, A148
Anderson, R. I., Koblischke, N. W., & Eyer, L. 2023, arXiv:2303.04790
Astropy Collaboration, Price-Whelan, A. M., Sipőcz, B. M., et al. 2018, AJ, 156, 123
Astropy Collaboration, Robitaille, T. P., Tollerud, E. J., et al. 2013, A&A, 558, A33
Beaton, R. L., Bono, G., Braga, V. F., et al. 2018, SSRv, 214, 113
Bellazzini, M., Ferraro, F. R., & Pancino, E. 2001, ApJ, 556, 635
Betoule, M., Kessler, R., Guy, J., et al. 2014, A&A, 568, A22
Blakeslee, J. P., Jensen, J. B., Ma, C.-P., Milne, P. A., & Greene, J. E. 2021, ApJ, 911, 65
Brout, D., Scolnic, D., Popovic, B., et al. 2022a, ApJ, 938, 110
Brout, D., Scolnic, D., Popovic, B., et al. 2022c, ApJ, 938, 24
Brout, D., Taylor, G., Scolnic, D., et al. 2022b, ApJ, 938, 111
Brown, P. J., Breeveld, A. A., Holland, S., Kuin, P., & Pritchard, T. 2014, Ap&SS, 354, 89
Brownsberger, S., Brout, D., Scolnic, D., Stubbs, C. W., & Riess, A. G. 2023, ApJ, 944, 188
Capozzi, F., & Raffelt, G. 2020, PhRvD, 102, 083007
Carr, A., Davis, T. M., Scolnic, D., et al. 2022, PASA, 39, e046
Choi, J., Dotter, A., Conroy, C., et al. 2016, ApJ, 823, 102
Dhawan, S., Goobar, A., Johansson, J., et al. 2022, ApJ, 934, 185
Dolphin, A. 2016, DOLPHOT: Stellar photometry, Astrophysics Source Code Library, ascl:1608.013
Freedman, W. L. 2021, ApJ, 919, 16
Freedman, W. L., Madore, B. F., Hatt, D., et al. 2019, ApJ, 882, 34
Freedman, W. L., Madore, B. F., Hoyt, T., et al. 2020, ApJ, 891, 57
Harris, C. R., Millman, K. J., van der Walt, S. J., et al. 2020, Natur, 585, 357
Hatt, D., Beaton, R. L., Freedman, W. L., et al. 2017, ApJ, 845, 146
Hoyt, T. J. 2023, NatAs, 7, 590
Hoyt, T. J., Beaton, R. L., Freedman, W. L., et al. 2021, ApJ, 915, 34
Hunter, J. D. 2007, CSE, 9, 90
Jang, I. S. 2023, MNRAS, 521, 1532
Jang, I. S., Hatt, D., Beaton, R. L., et al. 2018, ApJ, 852, 60
Jang, I. S., Hoyt, T. J., Beaton, R. L., et al. 2021, ApJ, 906, 125
Jang, I. S., & Lee, M. G. 2017, ApJ, 836, 74
Jones, D. O., Mandel, K. S., Kirshner, R. P., et al. 2022, ApJ, 933, 172
Kourkchi, E., Tully, R. B., Courtois, H. M., Dupuy, A., & Guinet, D. 2022, MNRAS, 511, 6160
Krisciunas, K., Contreras, C., Burns, C. R., et al. 2017, AJ, 154, 211
Lee, M. G., Freedman, W. L., & Madore, B. F. 1993, ApJ, 417, 553
Li, S., Casertano, S., & Riess, A. G. 2022, ApJ, 939, 96
Makarov, D., Makarova, L., Rizzi, L., et al. 2006, AJ, 132, 2729
McQuinn, K. B. W., Telidevara, A. K., Fuson, J., et al. 2021, ApJ, 918, 23
Ménard, B., Scranton, R., Fukugita, M., & Richards, G. 2010, MNRAS, 405, 1025
Méndez, B., Davis, M., Moustakas, J., et al. 2002, AJ, 124, 213
Mutlu-Pakdil, B., Sand, D. J., Crnojević, D., et al. 2022, ApJ, 926, 77
Pesce, D. W., Braatz, J. A., Reid, M. J., et al. 2020, ApJL, 891, L1
Peterson, E. R., Kenworthy, W. D., Scolnic, D., et al. 2022, ApJ, 938, 112
Planck Collaboration, Aghanim, N., Akrami, Y., et al. 2020, A&A, 641, A6
Radburn-Smith, D. J., de Jong, R. S., Seth, A. C., et al. 2011, ApJS, 195, 18
Riess, A. G., Yuan, W., Macri, L. M., et al. 2022, ApJL, 934, L7
Rose, B. M., Popovic, B., Scolnic, D., & Brout, D. 2022, MNRAS, 516, 4822
Salaris, M., & Cassisi, S. 1997, MNRAS, 289, 406
Schlafly, E. F., & Finkbeiner, D. P. 2011, ApJ, 737, 103
Scolnic, D., Brout, D., Carr, A., et al. 2022, ApJ, 938, 113
Scolnic, D., Casertano, S., Riess, A., et al. 2015, ApJ, 815, 117
Scolnic, D., Smith, M., Massiah, A., et al. 2020, ApJL, 896, L13
Scolnic, D. M., Jones, D. O., Rest, A., et al. 2018, ApJ, 859, 101
Serenelli, A., Weiss, A., Cassisi, S., Salaris, M., & Pietrinferni, A. 2017, A&A, 606, A33
Shaya, E. J., Tully, R. B., Pomarède, D., & Peel, A. 2022, ApJ, 927, 168
Shen, Z., Danieli, S., van Dokkum, P., et al. 2021, ApJL, 914, L12
Soltis, J., Casertano, S., & Riess, A. G. 2021, ApJL, 908, L5
Stetson, P. B. 1987, PASP, 99, 191
Tully, R. B., Kourkchi, E., Courtois, H. M., et al. 2023, ApJ, 944, 94
Tully, R. B., Rizzi, L., Shaya, E. J., et al. 2009, AJ, 138, 323
van der Walt, S., Colbert, S. C., & Varoquaux, G. 2011, CSE, 13, 22
Visser, M. 2004, CQGra, 21, 2603
Wu, J., Scolnic, D., Riess, A. G., et al. 2023, ApJ, 954, 87
Wu, P.-F., Tully, R. B., Rizzi, L., et al. 2014, AJ, 148, 7